

# Geophysical Research Letters®

## RESEARCH LETTER

10.1029/2021GL097262

We do not use the mineral name, dave-maoite, in spite of its IMA approval, because the article reporting presumed Ca-perovskite in a diamond inclusion (Tschauner et al., 2021) has been questioned by Walter et al. (2022a).

### Key Points:

- The Ca-perovskite (CaSiO<sub>3</sub>) melting curve determined to 136 GPa by four ab initio atomistic simulation methods
- A high melting temperature of about 7000 K at the core-mantle boundary suggests a wide liquidus field in the system CaO-MgO-SiO<sub>2</sub>
- Ca-perovskite is the first liquidus phase in basaltic compositions in the lowermost mantle

### Supporting Information:

Supporting Information may be found in the online version of this article.

### Correspondence to:

J.-A. Hernandez and C. E. Mohn,  
[jean-alexis.hernandez@esrf.fr](mailto:jean-alexis.hernandez@esrf.fr);  
[chrism@geo.uio.no](mailto:chrism@geo.uio.no)

### Citation:

Hernandez, J.-A., Mohn, C. E., Guren, M. G., Baron, M. A., & Trønnes, R. G. (2022). Ab initio atomistic simulations of Ca-perovskite melting. *Geophysical Research Letters*, 49, e2021GL097262. <https://doi.org/10.1029/2021GL097262>

Received 11 DEC 2021  
 Accepted 27 SEP 2022

© 2022. The Authors.

This is an open access article under the terms of the [Creative Commons Attribution License](#), which permits use, distribution and reproduction in any medium, provided the original work is properly cited.

## Ab Initio Atomistic Simulations of Ca-Perovskite Melting

J.-A. Hernandez<sup>1,2</sup>, C. E. Mohn<sup>1</sup>, M. G. Guren<sup>1,3</sup>, M. A. Baron<sup>1,4</sup>, and R. G. Trønnes<sup>1,5</sup>

<sup>1</sup>Centre for Earth Evolution and Dynamics, University of Oslo, Oslo, Norway, <sup>2</sup>Now at European Synchrotron Radiation Facility, Grenoble, France, <sup>3</sup>Now at Njord Centre, Department of Geoscience, University of Oslo, Oslo, Norway, <sup>4</sup>Now at Laboratoire de Chimie de la Matière Condensée de Paris, UMR 7574, Sorbonne Université, CNRS, Collège de France, Paris, France, <sup>5</sup>Natural History Museum, University of Oslo, Oslo, Norway

**Abstract** Melting curves of Ca-perovskite (pure CaSiO<sub>3</sub>) were determined by ab initio density functional theory, using two solid-liquid coexistence methods and two free energy approaches, in the form of thermodynamic integration and two-phase thermodynamics. The melting curves based on the solid-liquid coexistence methods and thermodynamic integration rise steeply from 2000 K at 14 GPa to 7000 K at 136 GPa. The melting temperature at 136 GPa is 1400 K higher than previous ab initio predictions. The high thermal stability of Ca-perovskite is linked to its high-symmetry isometric structure and consistent with experiments, demonstrating that Ca-perovskite is the most refractory phase in basaltic compositions in the lower mantle pressure range. The steep dT/dp slope of the melting curve also shows that the Ca-perovskite liquidus field expands relative to those of bridgmanite and silica with increasing pressure, in agreement with experimental evidence from simple and complex systems.

**Plain Language Summary** Melting of mantle minerals provides key information for understanding our planet's thermal evolution from the early stage of magma ocean crystallization to the present partial melting that is likely to occur near the core-mantle boundary. We determined the melting curve of Ca-perovskite (CaSiO<sub>3</sub>), the third most abundant mineral in the Earth's lower mantle, in a wide pressure range up to the core-mantle boundary pressure. Several atomistic simulation methods were used and show that Ca-perovskite melts about 2000 K higher than bridgmanite at the pressure conditions of lowermost mantle. This agrees with the experimental findings that Ca-perovskite is the last mineral to disappear when basaltic rocks undergo partial melting in the lower mantle.

## 1. Introduction

The lower mantle is dominated by the two silicate perovskites, bridgmanite and Ca-perovskite, constituting about 77 and 5 mol%, respectively, of peridotites and about 34 and 24 mol%, respectively, of recycled oceanic crust of basaltic composition (e.g., Stixrude & Lithgow-Bertelloni, 2012). The melting curves of the end member components MgSiO<sub>3</sub>, CaSiO<sub>3</sub> and MgO in the system CaO-MgO-SiO<sub>2</sub> system (CMS) may inform about the crystallization history of the magma ocean and the nature of the ultra-low velocity zones (e.g., Trønnes et al., 2021). Although the melting curves for MgO-periclase and MgSiO<sub>3</sub>-bridgmanite are reasonably well established through the lower mantle pressure range, the Ca-perovskite melting curve remains poorly constrained, in particular at the lowermost mantle pressures (Figure 1). The melting of Ca-perovskite at 14–15 and 16–60 GPa, respectively, has been investigated by multi-anvil (Gasparik et al., 1994) and laser-heated diamond anvil cell (LH-DAC) experiments (Shen & Lazor, 1995; Zerr et al., 1997). Multi-anvil experiments with resistive heating and W-Re thermocouples might provide more accurate and reproducible melting temperatures than the LH-DAC experiments, which are in poor agreement with each other with a difference in melting temperature of about 880 K at 45 GPa.

Nomura et al. (2017) performed multi-anvil experiments along the MgSiO<sub>3</sub>-CaSiO<sub>3</sub> join at 24 GPa and developed a thermodynamic model, anchored to the Zerr et al. (1997) melting curve. Although the experimentally based melting curves converge in the 2500–2800 K range at 14–16 GPa, the large variation in their dT/dp slopes yields increasing discrepancies with increasing pressure. The melting curve of Gasparik et al. (1994) is steeper (212 K/GPa in the 13–15 GPa range) than those determined by the LH-DAC experiments of Shen and Lazor (1995) and Zerr et al. (1997). The latter slopes, measured in the 17–20 GPa range are 32 and 61 K/GPa, respectively.

The Ca-perovskite melting curve has also been investigated by classical molecular dynamics (MD) based on empirical atomic potentials (Liu et al., 2010) and density functional theory (DFT) MD calculations (Braithwaite

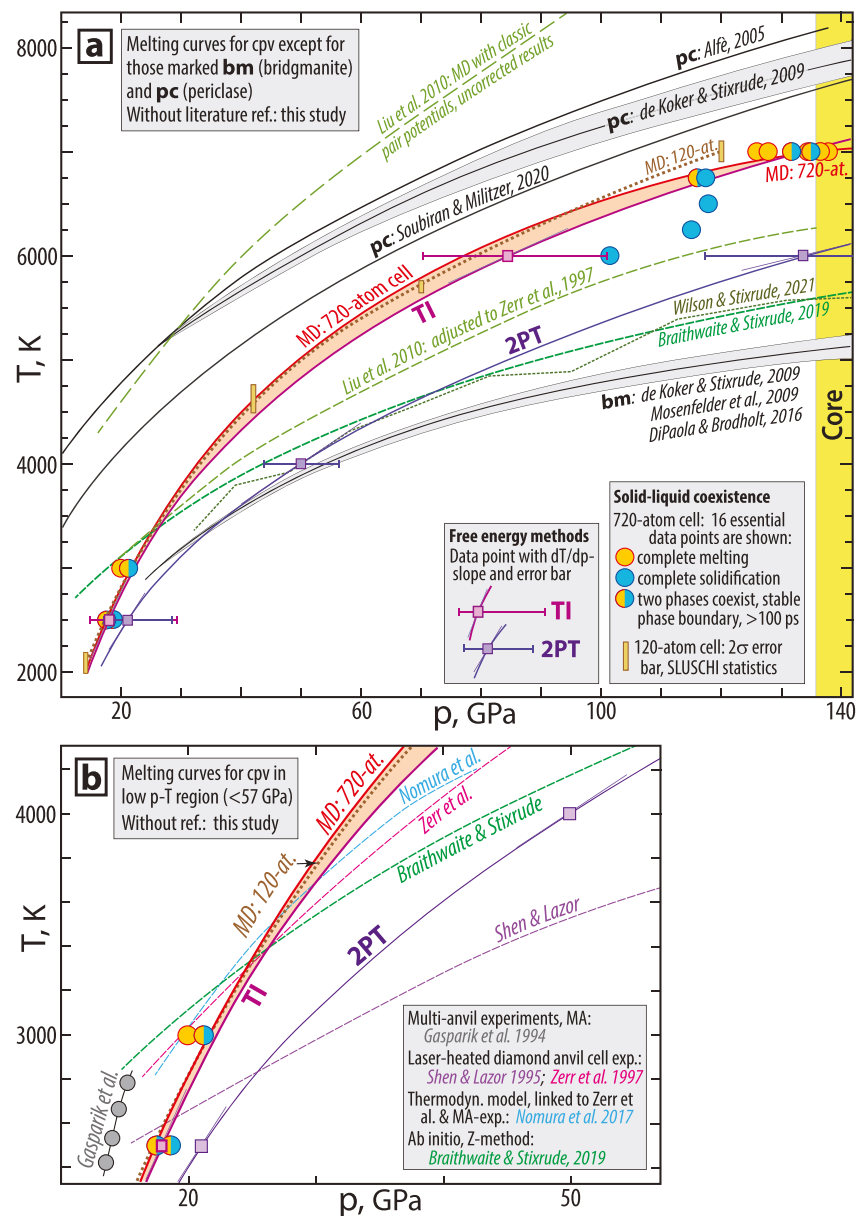


**Figure 1.** Melting curves for Ca-perovskite (cpv,  $\text{CaSiO}_3$ ), bridgmanite (bm,  $\text{MgSiO}_3$ ), and periclase (pc,  $\text{MgO}$ ) from previous determinations and this study. Our data points with individual uncertainties are listed in Tables S1 and S2 in Supporting Information S1. **Previously published melting curves:** (a) The  $\text{MgSiO}_3$  melting curve of de Koker and Stixrude (2009) has a gray uncertainty envelope, encompassing the melting curves of Mosenfelder et al. (2009) and Di Paola and Brodholt (2016). A corresponding  $\text{MgO}$  melting curve with a gray uncertainty envelope (de Koker and Stixrude, 2009) is shown together with the Alfè, 2005 and Soubiran and Militzer (2020) curves. Cpv-curves: Two melting curves, based on classic pair potential molecular dynamics (MD) simulation by Liu et al. (2010) include an upper curve, which is uncorrected for overheating, and a lower curve, corrected for 48% overheating by linking it to Zerr et al. (1997). The melting curves of Braithwaite and Stixrude (2019) and Wilson and Stixrude (2021) are based on the Z method and two-phase thermodynamics (2PT) method, respectively. (b) The gray circular symbols represent melting points determined by multi-anvil experiments by Gasparik et al. (1994). The curves from Shen and Lazor (1995) and Zerr et al. (1997) are based on one-sided laser-heated diamond anvil cell experiments, and the Nomura et al. (2017) curve is a thermodynamic model linked to 24 GPa multi-anvil experiments and the Zerr et al. (1997) curve. **The four different Ca-perovskite melting curves from this study** include curves based on 2PT, thermodynamic integration for the melt, combined with 2PT-method free energy for Ca-perovskite (labeled TI), as well as MD solid-melt coexistence simulations with 120- and 720-atom cells (small and large cells). Orange shading marks the p-T region between the 720-atom cell and thermodynamic integration (TI) curves. The TI and 2PT curves are Simon and Glatzel (1929) regressions based on the melting points and their dp/dT slopes. The 120- and 720-atom cell solid-liquid coexistence curves are drawn with a smooth cubic spline-like function, with the 720-atom cell curve weighted by the point clusters at 18–21 GPa and 116–135 GPa.

& Stixrude, 2019; Wilson & Stixrude, 2021). The classical MD study was carried out by heating homogeneously until melting at a critical temperature,  $T_h$ , which is much higher than the equilibrium melting temperature,  $T_m$ . The melting curve was therefore adjusted by a constant shift,  $T_m = 0.48 \times T_c$ , in the entire pressure-range, to coincide with the melting temperature reported at 24 GPa by Zerr et al. (1997). A similar approach was used in the DFT-MD study using the Z-method of Belonoshko et al. (2006), where the melting curve was estimated from a series of MD runs in the micro-canonical (NVE) ensemble (Braithwaite & Stixrude, 2019). The simulated system is heated in steps to slightly above  $T_h$  where the systems start to melt homogeneously. Temperature drops as more solid is gradually transformed to liquid until all remaining solid has eventually melted at a temperature near  $T_m$ . The cooling toward  $T_m$  may be slow, and therefore the Z-method provides, in theory, an upper bound for the melting temperature. In a recent ab initio study, Wilson and Stixrude (2021) used a two-phase thermodynamics (2PT) method where free energies of liquid and solid phases are estimated separately based on the partial vibrational power spectra of the different atomic species and the melting curve is located at p-T-conditions of equal Gibbs free energies. The resulting ab initio melting curve from 2PT is in good agreement with that of the Z-method (Braithwaite & Stixrude, 2019) but lie at a markedly lower temperature (above 43 GPa) compared to Liu et al. (2010). Although Braithwaite and Stixrude (2019) did not report any melting point below 43 GPa, extrapolation of their melting curve to 14 GPa lies above experimental ones in the 15–20 GPa range.

These discrepancies, and the potentially important role of Ca-perovskite as a high-density residual mineral during melt-solid separation in the lowermost mantle (e.g., Pradhan et al., 2015; Tateno et al., 2018; Trønnes et al., 2021), motivated us to determine the Ca-perovskite melting curve to lowermost mantle pressure conditions using DFT atomistic simulations. A well-defined melting curve for Ca-perovskite will improve thermodynamic models predicting the phase relations for lower mantle lithologies and have important consequences for materials, structures and dynamics of the lowermost mantle. We explored four complementary methods to calculate the melting curve of  $\text{CaSiO}_3$  in the entire lower mantle pressure regime. Two of these methods started with simulation boxes containing coexisting liquid and solid phases in mechanical contact. In addition, we explored two free energy methods, in which energies of the solid and liquid phases were calculated from separate one-phase simulation boxes to obtain the melting curve. We also used the Z-method to compare directly with the melting curve of Braithwaite and Stixrude (2019).

## 2. Methods and Theory

### 2.1. Solid-Liquid Coexistence Calculations

In the two solid-liquid coexistence methods, molecular dynamics calculations were launched with solid and liquid phases in mechanical contact. The small-cell coexistence method uses cells with typically between 100 and 200 atoms (Hong & Van De Walle, 2016), and the melting temperature is based on a statistical distribution of the number of simulations ending up as solid or liquid. The large-cell coexistence method (e.g., Alfè, 2005), involving more than 400 atoms, aims to determine the equilibrium pressure or temperature in a single MD run with a stable solid-liquid phase boundary and to bracket the melting curve with additional MD runs ending as solid or liquid phases.

#### 2.1.1. Large-Cell Solid-Liquid Coexistence Approach

The MD calculations were launched in an appropriate ensemble from an initial configuration of atoms consisting of one solid and one liquid part. In the NVT ensemble with fixed volume and temperature, pressure is allowed to drift during the run, and the fraction of solid and liquid changes as the system equilibrates. If the initial pressure is lower than the melting pressure (with  $\rho_{\text{solid}} > \rho_{\text{liquid}}$ ,  $\rho$  is density), the solid-liquid interface adjusts to increase the fraction of liquid as the system equilibrates, thereby increasing the pressure toward the melting curve. Similarly, if the MD run is launched with a pressure that is higher than the melting pressure (with  $\rho_{\text{solid}} < \rho_{\text{liquid}}$ ), the solid fraction of the box increases and the pressure decreases toward the melting curve as the system equilibrates. After equilibration, the pressure fluctuates around a fixed value, the melting pressure, and the phase boundary separating the solid and liquid does not drift (Figure S1 in Supporting Information S1). However, if the initial conditions are too far from equilibrium (highly strained or initial temperature and pressure too far from the melting curve), the simulation may “collapse” to a single solid or liquid phase (Figure S1 in Supporting Information S1). To avoid this, large simulation boxes containing several thousands of atoms are required, but such calculations are computationally too expensive at the DFT level. However, we can still bracket the melting curve by a series of

calculations at different temperatures, using a smaller cell (containing typically between 400 and 1000 atoms). Both the number of simulations ending up in a solid or liquid phase and how quickly they melt or freeze provide important constraints on the melting temperature. This is also a key idea in the small-cell coexistence approach discussed below.

A number of ab initio studies have demonstrated the success of the large-cell solid-melt coexistence methods for computing melting curves (Morris et al., 1994). Alfè, 2005 used DFT together with MD to predict the melting curve of MgO periclase to lowermost mantle conditions. Because calculations may suffer from slow kinetics, in particular if an MD run is launched close to the melting point, Di Paola and Brodholt (2016) used a combination of pair potentials and ab initio MD to predict accurately the melting curve of MgSiO<sub>3</sub> bridgmanite.

### 2.1.2. Small Size Two-Phase Coexistence Approach

A different approach has recently been developed in an attempt to reduce the overall computational cost of solid-liquid coexistence MD simulations to calculate the melting temperature (Hong & Van De Walle, 2016). Rather than carrying out a single MD calculation in a large (>400-atom) simulation cell, several MD runs are performed in a much smaller simulation box containing up to 200 atoms. MD runs carried out in such a small box do not equilibrate with an intact liquid-solid phase boundary, but rapidly (typically within a few ps) collapse into a single solid or single liquid phase due to thermal fluctuations (Figure S2 in Supporting Information S1). The melting point is then calculated from a probability distribution of the number of simulations ending up as a solid or a liquid phase. If the number of calculations ending up as solid and liquid phases are equal, the simulation temperature equals the melting temperature. By carrying out solid-liquid coexistence calculations at several different temperatures, the melting curve can be found from a fitting procedure using appropriate thermodynamic relations as discussed in Hong and Van De Walle (2016). Even if it requires multiple runs, the relatively small simulation boxes shorten the computational cost considerably compared to the large-cell approach. However, it requires careful quantification of finite-size effects, as the phase boundary volume is similar to those of the solid and liquid phases.

## 2.2. Free Energy Approaches

### 2.2.1. Thermodynamic Modeling Based on the Velocity Autocorrelation Function

The third approach we used to determine the melting curve is based on free energy calculations of the solid and liquid phases in separate simulation boxes using a two-phase thermodynamics (2PT) method (Desjarlais, 2013; Lai et al., 2012; Lin et al., 2003). For a given temperature and volume, the individual contributions (vibrational, electronic, etc.) to the Gibbs (or Helmholtz) free energy of the solid are calculated separately. The melting curve is then obtained by finding the pressure at which the Gibbs free energies of the solid and liquid are equal along several isotherms.

For a given phase, we consider:

$$g = u_{\text{MD}} + u_{\text{qc}} + pV - T(s_{\text{el}} + s_{\text{ion}}) \quad (1)$$

where  $u_{\text{MD}}$ ,  $u_{\text{qc}}$ ,  $p$ ,  $V$ ,  $T$ ,  $s_{\text{el}}$  and  $s_{\text{ion}}$  are the internal energy from the DFT-MD, an energy correction for the nuclear quantum effects (NQE), the pressure, volume, temperature, and electronic and ionic entropies of the system, respectively. The use of small letters for the internal energy and the entropy indicate the energy per mass unit. At given  $V$  and  $T$ , the internal energy ( $u_{\text{MD}}$ ), electronic entropy ( $s_{\text{el}}$ ) and temperature are straightforwardly obtained from the DFT-MD. The ionic entropy ( $s_{\text{ion}}$ ), assumed to be equal to the vibrational entropy, and the correction to the internal energy ( $u_{\text{qc}}$ ) for NQE, are determined based on partial vibrational power spectra obtained from the atomic trajectories (see Supplementary Information for more details).

In the 2PT approach we assume that the vibrational density of states is divided into solid-like and gas-like contributions. It may therefore be less accurate than other free energy approaches, such as thermodynamic integration, where no such assumptions are imposed. The advantage with the 2PT method, however, is that it is computationally cheaper, has a flexible theoretical framework, does not rely on complex simulation paths and provides insights into the trends and relations between the atom dynamics and the entropy.

### 2.2.2. Thermodynamic Integration

In a fourth approach, we determine the Gibbs free energy of the liquid phase, using the thermodynamic integration (TI) technique, to determine free energies.

The Helmholtz free energy of the liquid ( $F_{\text{liquid}}$ ) is found by direct thermodynamic integration between the DFT liquid and the reference ideal gas, which leads to (Dorner et al., 2018):

$$F_{\text{liquid}}(V, T) = F_{IG}(V, T) + \Delta F_{IG \rightarrow \text{DFT}}(V, T) = F_{IG}(V, T) + \int_0^1 \langle U_{\text{DFT}} \rangle_\lambda d\lambda \quad (2)$$

However,  $\langle U_{\text{DFT}} \rangle_\lambda$  cannot be evaluated when  $\lambda$  is equal or close to 0 as the atoms largely overlap. To constrain the integration at  $\lambda = 0$ , we define a new variable,  $x$ , such that  $\lambda = \left(\frac{x+1}{2}\right)^{\frac{1}{1-k}}$  with  $k = 0.8$  (Dorner et al., 2018; Yuan & Steinle-Neumann, 2020). This was previously used for melting simulations of Si and  $\text{MgSiO}_3$ . The integral can be rewritten as:

$$\int_0^1 \langle U_{\text{DFT}} \rangle_\lambda d\lambda = \frac{1}{2(1-k)} \int_{-1}^1 \langle U_{\text{DFT}} \rangle_x \left(x + \frac{1}{2}\right)^{\frac{k}{1-k}} dx \quad (3)$$

and  $(V, T)$  is computed from its known analytical expression:

$$F_{IG}(V, T) = - \sum_i k_B T \ln \left( \frac{V^{N_i}}{\Lambda_i^{3N_i} N_i!} \right) \quad (4)$$

where  $i$  represents a given species,  $N_i$  is the number of atoms of this species, and  $\Lambda_i = h / \sqrt{2\pi N_i m_i k_B T}$  is the thermal de Broglie wavelength with  $h$  being the Planck constant and  $m_i$  the mass of species  $i$ .

The Gibbs free energy,  $G$ , of the system, is obtained from  $F$  and the pressure  $p$  calculated in the pure DFT-MD system. The specific Gibbs free energies of the liquid computed with TI, and of the solid computed previously from 2PT, are then compared as functions of pressure to determine the melting pressure at a given temperature. The errors on the melting pressures are obtained by considering a representative error of 0.1 kJ/g on the Gibbs free energy estimate.

Computational details related to the solid-liquid coexistence and free energy approaches are given in Section S1 in Supporting Information S1, and the procedures for our additional Z-method calculations are given in Section S2 in Supporting Information S1.

### 2.2.3. Z Method

Our implementation of the Z-method follows Belonoshko et al. (2006), where the melting temperature is estimated from a series of MD runs in the NVE ensemble. To ensure realistic conservative dynamics we explore different strategies in calculating the electronic entropy in a variable temperature ensemble (NVE). In one of these, the electronic entropy is updated frequently along the ionic trajectory which ensures that the ionic kinetic energy plus the electronic free energy is conserved (Wentzcovitch et al., 1992). This avoids premature melting and drift in the total energy which may hamper the Z method if the electronic temperature is very different from the ionic temperature. We have described in detail our implementation of the Z-method in Text S2 in Supporting Information S1 and results are reported in Table S2 in Supporting Information S1.

## 3. Melting Curves, Entropy and Kinetics of Melting

Our Ca-perovskite melting curves from the two solid-liquid coexistence methods and thermodynamic integration differ by less than 220 K in the entire 14–139 GPa pressure range (Figure 1 and Figure S1 in Supporting Information S1). The Z-method melting temperature, derived with the same parameters as in Braithwaite and Stixrude (2019), is consistent with these curves, bearing in mind that the method only provides an upper bound



for the equilibrium melting temperature. The melting curve from the 2PT approach in both solid and liquid is markedly lower than the other three melting curves.

In the low-pressure range (14–20 GPa), the melting curves from thermodynamic integration in the liquid (TI) and the two solid-liquid coexistence methods are parallel and differ by 130–150 K, only. At 2400 K, the intermediate TI-curve is 3.8 GPa higher than the slightly steeper Gasparik et al. (1994) curve. The multi-anvil experiments of Gasparik et al. (1994), which were carried out in a well-controlled sample domain in their standard 10–5 mm pressure cell configuration with W-Re thermocouples, are highly reproducible. The pressure calibration, however, was performed at temperatures of 1473–1873 K (Gasparik, 1989), which are almost 1000 K lower than the Ca-perovskite melting temperatures of 2400–2800 K. We therefore speculate that most of the offset between the lower Gasparik et al. (1994) pressures and our higher pressures in the 2400–2800 K range might result from a thermal pressure effect (e.g., Andraut et al., 1988), which is normally ignored in multi-anvil experiments. The larger  $dT/dp$  slope the Gasparik et al. (1994) melting curve can also be explained by increasing thermal pressure with increasing temperature. An important caveat, however, is that even if multianvil and laser-heated diamond anvil cell experiments are fraught by several sources of uncertainties, the GGA functional used in our *ab initio* simulations generally underbinds and may therefore underestimate the melting-temperature (Zhu et al., 2020).

Ignoring 2PT, the other three melting curves are quasi-parallel and rise steeply from about 2400 K at 17 GPa, to 6000 K at 80 GPa and 7020 K at 136 GPa. The associated  $dT/dp$  slopes decrease with increasing pressure. The 2PT melting point of 6025 K is about 1000 K lower than the other melting curves at 136 GPa, but only 440 K above the 2PT curve of Wilson and Stixrude (2021) and the Z-method curve of Braithwaite and Stixrude (2019). The energies computed in the liquid from the TI compared to the 2PT method, indicate that the low 2PT melting curve can be explained by an overestimation of the melt entropy, which in turn underestimates the Gibbs free energy of the melt (Figures S5 and S6 in Supporting Information S1).

To examine the discrepancy between our melting curves and the Z-method curve of Braithwaite and Stixrude (2019), we have analyzed possible systematic errors associated with simulation cell size and slow kinetics, which may hamper full equilibration in the solid-liquid coexistence calculations. Small simulation cells may be unable to capture the slow dynamics of melting involving cooperative excitations of polymerized long chains. Comparison of small-cell calculations carried out using 80-, 120-, and 240-atom cells shows that the melting temperature from the 80-atom runs is higher than those from the 120-atom and 240-atom simulations (Figure S7 in Supporting Information S1). At 80 and 120 GPa, for example, the 80-atom runs melt at about 350 and 450 K higher, respectively, than the 240-atom cell, whereas the difference in melting point between the 120- and 240-atom cell was less than 100 K at 120 GPa. This is also supported by the comparison of results from small- and large-cell calculations and how quickly they melt or freeze. The large-cell solid-liquid calculations launched at 6750 K had an intact solid-liquid boundary after 100 ps, whereas the small-cell calculations at 6700 K and 120 GPa froze completely within a few ps. The difference between the small-cell and large-cell calculations may therefore partly be due to cell size effects, but comparison of 120 and 240 atom simulations indicate that these are less than 200 K.

The good agreement between the small-cell and large-cell results, is possibly explained by the sharp solid-liquid boundary with small interphase-volume in the optimally designed small cells. Comparison of results from the different cell sizes suggests that even the small 120-atom cells are sufficiently large to capture structural correlation required to trigger melting near the  $T_m$  calculated using large cells.

The kinetics of melting must be considered in a comparison between the free energy and solid-liquid coexistence methods. Slow kinetics may prevent equilibration during the solid-liquid coexistence simulations, in particular if MD runs are started near or below the melting temperature. Such effects were investigated by Di Paola and Brodholt (2016), who determined the melting curve of bridgmanite using the large-cell solid-liquid coexistence method. For MD runs launched near the melting temperature, a migration of the solid-liquid interface was difficult to detect, even in a long (>100 ps) trajectory. It was shown that the relaxation time during equilibration follows a two-body exponential kinetic decay model, reflecting much slower kinetics in simulations launched close to the melting temperature (i.e., 100 K or less above  $T_m$ ), compared to simulations initiated more than 250 K above  $T_m$ . Since we used a similar cell-size to Di Paola and Brodholt (2016), it is useful to compare the relaxation of the boundary in our large-cell solid-liquid coexistence calculations with that of bridgmanite. Two MD simulations performed at 7500 and 7000 K with final pressures of 127.8 and 125.9 GPa, respectively (Table

S1 in Supporting Information S1) melted rapidly, within less than 3 and 12 ps. The MD run at 6750 K with final pressure of 116.0 GPa, however, had intact solid-liquid boundary without visible drift for 100 ps. If we assume that Ca-perovskite melting follows a similar kinetic decay model as bridgmanite, the long MD runs carried out at 6750 K should deviate by less than 250 K from the “true” melting curve. All of the large-cell solid-liquid coexistence calculations initiated above 100 GPa at temperatures at or below 6500 K ended up as solids (Table S1 in Supporting Information S1), suggesting a strict lower bound to the melting temperature of Ca-perovskite of 6500 K at 120 GPa.

The large- and small-cell solid-liquid coexistence MD-calculations carried out below  $T_m$  often formed simple defects and frozen-in glass-like clusters in the initially liquid part the simulation box (Figure S1 in Supporting Information S1). Even in simulations slightly below  $T_m$ , glass-like clusters would eventually form, especially at high-pressure. The low melting curve derived by the Z-method in the NVE ensemble (Braithwaite & Stixrude, 2019) might be related to the transition from the homogeneous molten state to a glass-like state, rather than to a solid, during cooling. Such an outcome might be related to the lower system kinetic energy (and hence temperature) for the glass-like state than for the fully molten liquid state, analogous to the glass transition, which is lower than the melting temperature. To see if glass-like clusters may hamper the Z-method, we have used this approach to investigate the liquid structure near the melting point. Computational details and results from these runs are reported in Section S2 and Table S2 in Supporting Information S1. Inspection of the trajectories does not reveal evidence of glass or glass-like cluster at the final state along the isochore when the solid melts homogeneously (i.e., near  $T_m$ ). Although we used the same computational details as those of Braithwaite and Stixrude (2019), we are unable to reproduce the homogeneous and equilibrium melting points and thus cannot rule out that a glassy state might have formed in their simulations. Using our Z method and the same pseudo-potentials, functional, energy cut-off and cell-size, our calculated  $T_h$  is 8806 K at 105 GPa, which is roughly 1700 K higher than 7120 K at 103 GPa found by Braithwaite and Stixrude (2019). Calculations using a similar waiting time analysis as that of Braithwaite and Stixrude (2019) gave a  $T_m$  of 6493 K at 105 GPa, about 1300 K higher than that reported by Braithwaite and Stixrude (2019) at the same density. To compare directly with the results reported in Figure 1, we also carried out Z-method calculations using the PBE functional with similar input parameters for the electronic wave function as we used in the two-phase calculations. The resulting melting temperature at 104.8 GPa is 6589 K, in good agreement with our melting curves in Figure 1.

The difference between our 2PT melting curve (especially above 6000 K) and that reported in Wilson and Stixrude (2021) likely comes from the remaining difference in the entropy of the melt. In particular, at 6000 K, the difference of  $\sim 0.7$  kJ/g in  $T_s$  (Figure S6 in Supporting Information S1) will shift the melting pressure from 133 to 208 GPa, very close to the 2PT curve of Wilson and Stixrude (2021). Around 30% of this difference is due to a difference in the electronic entropy, which could be related to the use of different exchange-correlation functionals (PBE vs. PBEsol). The rest could be due to the cell size (320 atoms in our study vs. 135 atoms in Wilson & Stixrude, 2021) or slightly different dynamics in the PBE and PBEsol systems. In order to compare our results with available experimental data (Richet et al., 1991), we computed the entropy of  $\text{CaSiO}_3$  melt at 2000 K and ambient density using the 2PT approach. We found  $T_s \sim 6.13$  kJ/g, which is 0.28 kJ/g larger than the experimental value 5.85 kJ/g obtained at by Richet et al. (1991), and lower than the 6.30 kJ/g obtained in Wilson and Stixrude (2021). The  $\sim 3\%$  difference between the Wilson and Stixrude (2021) and our 2PT data is also observed at 4000 and 6000 K, indicating our 2500 K data point is consistent with all other 2PT data obtained in this study at different temperatures.

Similarly, the difference between our 2PT and TI data is  $\sim 2.5\%$  at both 2500 and 6000 K and is also quasi-independent of density. If this difference remains the same at 2000 K, the  $T_s$  term obtained from TI would be  $\sim 5.98$  kJ/g, that is, 0.13 kJ/g larger than the experimental value, close to the  $\pm 0.1$  kJ/g accuracy for the Gibbs free energy obtained from our simulations. In Ca-perovskite, the 2PT approach gives entropies in good agreement with the 2PT results from Wilson and Stixrude (2021). Although the choice of the functional influences the EOS of both phases (Figure S6 in Supporting Information S1), the relative volume difference between the solid and the liquid phases is similar between PBE and PBEsol, resulting in a minor influence on the melting conditions.

Our four different ab initio approaches to determine the melting curve of Ca-perovskite through the lower mantle pressure range are all independent of previous experimental and theoretical studies. Figure 1a shows that our Ca-perovskite melting curves have steeper  $dT/dp$ -slopes than the  $\text{MgO}$  and  $\text{MgSiO}_3$  end-members of periclase and bridgmanite in the 20–80 GPa range (Alfè, 2005; de Koker and Stixrude, 2009; Di Paola and Brodholt, 2016;

Mosenfelder et al., 2009; Soubiran & Militzer, 2020). At 24 GPa, the bridgmanite melting temperature of 2890 K is only 290 K lower than that of Ca-perovskite (the TI curve is at 3180 K), whereas periclase melts 1200–1800 K higher at 4400–5000 K (Figure 1). At the CMB pressure, the order of the melting temperatures of the three phases is the same. Here the TI melting curve of Ca-perovskite is only 570–1130 K lower than the periclase melting curves of Soubiran and Militzer (2020) and Alfè (2005), respectively, but 1900–2000 K higher than the bridgmanite curves of de Koker and Stixrude (2009), Mosenfelder et al. (2009) and Di Paola and Brodholt (2016).

The strong pressure-induced increase in the thermal stability of Ca-perovskite compared to that of bridgmanite might be related to the more symmetric crystal structure of the isometric Ca-perovskite compared to the orthorhombic bridgmanite. The more ideal and adaptive Ca-perovskite structure is also reflected by the lack of a post-perovskite form of  $\text{CaSiO}_3$ , which instead decomposes to pyrite-structured  $\text{SiO}_2$  and B2-structured CaO at 580–610 GPa and 2500–2750 K (Tsuchiya & Tsuchiya, 2011).

#### 4. Implications for Phase Relations and Dynamics of the Lowermost Mantle

The high and steeply rising melting curve of Ca-perovskite prescribes a compositionally extensive liquidus field, expanding with increasing pressure. This inference is supported by the observed liquidus phase relations of basaltic compositions for the lower mantle pressure range. Based on experimentally determined phase relations in basaltic and peridotitic compositions and along the  $\text{MgO-SiO}_2$  and  $\text{MgSiO}_3\text{-CaSiO}_3$  joins, Trønnes et al. (2019) constructed cotectic lines and eutectic points separating the liquidus fields of ferropericlase, bridgmanite, silica and Ca-perovskite in the pseudoternary system CMS at 24–136 GPa. The components, calculated from cation%, have been slightly revised to  $C = \text{Ca} + \text{Na} + \text{K}$ ,  $S = \text{Si} + 0.9 \text{ Al}$  and  $M = 100 - (C + S)$ . The pseudoternary projection diagrams demonstrate how the liquidus field of Ca-perovskite increases with increasing pressure, as the periclase-bridgmanite and bridgmanite-silica eutectics in the simple  $\text{MgO-SiO}_2$  system move toward MgO and  $\text{SiO}_2$ , respectively (de Koker et al., 2013; Liebske & Frost, 2012; Ohnishi et al., 2017; Ozawa et al., 2018; Yao et al., 2021), and the cotectic boundary separating the Ca-perovskite from the bridgmanite or post-bridgmanite fields moves toward bridgmanite or post-bridgmanite (Pradhan et al., 2015; Tateno et al., 2018). Our new melting curve for the Ca-perovskite endmember component may facilitate improved thermodynamic modeling of the liquidus phase relations in the system  $\text{CaO-MgO-SiO}_2$ .

Based on their low melting curve, Braithwaite and Stixrude (2019) inferred that the Ca-perovskite-bridgmanite eutectic on the  $\text{MgSiO}_3\text{-CaSiO}_3$  join would move toward  $\text{CaSiO}_3$  with increasing pressure. With our higher melting curve, the binary eutectic would move in the opposite direction. The ternary pseudo-eutectic melts coexisting with assemblages of bridgmanite (or post-bridgmanite), silica and Ca-perovskite at 58–135 GPa, determined by Pradhan et al. (2015) and Tateno et al. (2018), confirm this displacement. The high thermal stability of Ca-perovskite in the lowermost mantle have important consequences for the crystallisation of the basal magma ocean with incorporation of this dense phase into late-stage cumulates that later might be convectively swept into the base layers of the large low S-wave velocity provinces (LLSVPs). Partial melting and disaggregation of recycled oceanic crust in the hottest regions near the CMB, followed by sinking of dense pseudo-eutectic melts and residual Ca-perovskite, may also result in Ca-perovskite enrichment in the ultra-low velocity zones (Trønnes et al., 2021).

Ca-perovskite in peridotitic and basaltic lithologies, as well as in diamond inclusions, has a limited compositional deviation from  $\text{CaSiO}_3$  with each of the minor elements, Ti, Al, Fe, Mg and Na, generally comprising less than 2 cation% (e.g., Corgne et al., 2005; Tateno et al., 2018; Walter et al., 2011; Walter, Thomson, & Smith, 2022; Section S3 in Supporting Information S1). The experimentally determined partition coefficients between Ca-perovskite and peridotitic melts for the trivalent and quadrivalent lithophile elements with ionic radii similar to U, Th and the middle to heavy lanthanides at about 24 GPa are extremely high, in the range of 10–25 (e.g., Corgne et al., 2005; Corgne & Wood, 2005). Even if corresponding partition coefficients at pressures corresponding to the deepest part of the lower mantle have not been fully explored, they are very likely to exceed unity. The incorporation of large amounts of U (up to 4 atom%) in Ca-perovskite has been experimentally documented at up to 54 GPa (Greux et al., 2009). The experimental results of Corgne et al., 2005 in combination with ab initio results of Deng and Stixrude (2021), indicate that the bridgmanite-melt partition coefficient for the compatible element Hf increases from 1.4 at 24 GPa and 2600 K to 5.3 at 136 GPa and 4000 K. The mineral-melt partition coefficients for compatible high-field strength elements in Ca-perovskite might show comparable variation in the same p-T range. High contents of U- and Th-rich Ca-perovskite in the LLSVPs and ULVZs have



profound consequences for the production of heat, radiogenic He and nucleogenic Ne in the root zones of the major mantle plumes. The primordial-like  $^3\text{He}/^4\text{He}$  signal and the solar Ne-isotopic composition found in several plume-derived ocean island basalts (e.g., White, 2015) are therefore unlikely to be sourced in the LLSVP base layers or in the ULVZs.

## Data Availability Statement

Data produced in this study are available in Supporting Information S1 and at <https://osf.io/982vn>, together with the implementation of the 2PT model used in this study.

## Acknowledgments

The Centre for Earth Evolution and Dynamics is funded by the Research Council of Norway through its Centre of Excellence program (Grant 223272). Computational resources were provided by the Norwegian infrastructure for high-performance computing (NOTUR, Sigma-2, Grants NN9329K and NN2916K). We thank John Brodholt for discussions and good advice. Perceptive comments and useful suggestions by two reviewers led to additional investigations and a major improvement of the article.

## References

- Alfè, D. (2005). Melting curve of MgO from first-principles simulations. *Physical Review Letters*, 94(23), 4–7. <https://doi.org/10.1103/physrevlett.94.235701>
- Andrault, D., Fiquet, G., Ité, J.-P., Richet, P., Gillet, P., Häusermann, D., & Hanfland, M. (1998). Thermal pressure in the laser-heated diamond-anvil cell: An X-ray diffraction study. *European Journal of Mineralogy*, 10(5), 931–940. <https://doi.org/10.1127/ejm/10/5/0931>
- Belonoshko, A. B., Isaev, E. I., Skorodumova, N. V., & Johansson, B. (2006). Stability of the body-centered-tetragonal phase of Fe at high pressure: Ground-state energies, phonon spectra, and molecular dynamics simulations. *Physical Review B*, 74(21), 214102. <https://doi.org/10.1103/physrevb.74.214102>
- Braithwaite, J., & Stixrude, L. (2019). Melting of  $\text{CaSiO}_3$  perovskite at high pressure. *Geophysical Research Letters*, 46(4), 2037–2044. <https://doi.org/10.1029/2018gl081805>
- Corgne, A., Liebske, C., Wood, B. J., Rubie, D. C., & Frost, D. J. (2005). Silicate perovskite-melt partitioning of trace elements and geochemical signature of a deep perovskitic reservoir. *Geochimica et Cosmochimica Acta*, 69(2), 485–496. <https://doi.org/10.1016/j.gca.2004.06.041>
- Corgne, A., & Wood, B. J. (2005). Trace element partitioning and substitution mechanisms in calcium perovskites. *Contributions to Mineralogy and Petrology*, 149(1), 85–97. <https://doi.org/10.1007/s00410-004-0638-3>
- de Koker, N., Karki, B. B., & Stixrude, L. (2013). Thermodynamics of the  $\text{MgO-SiO}_2$  liquid system in Earth's lowermost mantle from first principles. *Earth and Planetary Science Letters*, 361, 58–63. <https://doi.org/10.1016/j.epsl.2012.11.026>
- de Koker, N., & Stixrude, L. (2009). Self-consistent thermodynamic description of silicate liquids, with application to shock melting of MgO periclase and  $\text{MgSiO}_3$  perovskite. *Geophysical Journal International*, 178(1), 162–179. <https://doi.org/10.1111/j.1365-246x.2009.04142.x>
- Deng, J., & Stixrude, L. (2021). Deep fractionation of Hf in a solidifying magma ocean and its implications for tungsten isotopic heterogeneities in the mantle. *Earth and Planetary Science Letters*, 562, 116873. <https://doi.org/10.1016/j.epsl.2021.116873>
- Desjarlais, M. P. (2013). First-principles calculation of entropy for liquid metals. *Physical Review E*, 88(6), 062145. <https://doi.org/10.1103/physreve.88.062145>
- Di Paola, C., & Brodholt, J. P. (2016). Modeling the melting of multicomponent systems: The case of  $\text{MgSiO}_3$  perovskite under lower mantle conditions. *Scientific Reports*, 6(1), 29830. <https://doi.org/10.1038/srep29830>
- Dorner, F., Sukurma, Z., Dellago, C., & Kresse, G. (2018). Melting Si: Beyond density functional theory. *Physical Review Letters*, 121(19), 195701. <https://doi.org/10.1103/physrevlett.121.195701>
- Gasparik, T. (1989). Transformation of enstatite-diopside-jadeite pyroxenes to garnet. *Contributions to Mineralogy and Petrology*, 102(4), 389–405. <https://doi.org/10.1007/bf00371083>
- Gasparik, T., Wolf, K., & Smith, C. M. (1994). Experimental determination of phase determination in the  $\text{CaSiO}_3$  system from 8 to 15 GPa. *American Mineralogist*, 79, 1219–1222.
- Greaux, S., Gautron, L., Andrault, D., Bolfan-Casanova, N., Guignot, N., & Bouhifd, M. A. (2009). Experimental high pressure and high temperature study of the incorporation of uranium in Al-rich  $\text{CaSiO}_3$  perovskite. *Physics of the Earth and Planetary Interiors*, 174(1–4), 254–263. <https://doi.org/10.1016/j.pepi.2008.06.010>
- Hong, Q. J., & Van De Walle, A. (2016). A user guide for SLUSCHI: Solid and liquid in ultra small coexistence with hovering interfaces. *Calphad Computer Coupling of Phase Diagrams and Thermochemistry*, 52, 88–97. <https://doi.org/10.1016/j.calphad.2015.12.003>
- Lai, P. K., Hsieh, C. M., & Lin, S. T. (2012). Rapid determination of entropy and free energy of mixtures from molecular dynamics simulations with the two-phase thermodynamic model. *Physical Chemistry Chemical Physics*, 14(43), 15206–15213. <https://doi.org/10.1039/c2cp42011b>
- Liebske, C., & Frost, D. J. (2012). Melting phase relations in the  $\text{MgO-MgSiO}_3$  system between 16 and 26 GPa: Implications for melting in Earth's deep interior. *Earth and Planetary Science Letters*, 345–348, 159–170. <https://doi.org/10.1016/j.epsl.2012.06.038>
- Lin, S. T., Blanco, M., & Goddard, W. A. (2003). The two-phase model for calculating thermodynamic properties of liquids from molecular dynamics: Validation for the phase diagram of Lennard-Jones fluids. *Journal of Chemical Physics*, 119(22), 11792–11805. <https://doi.org/10.1063/1.1624057>
- Liu, Z. J., Yan, J., Duan, S. Q., Sun, X. W., Zhang, C. R., & Guo, Y. (2010). The melting curve of  $\text{CaSiO}_3$  perovskite under lower mantle pressures. *Solid State Communications*, 150(13–14), 590–593. <https://doi.org/10.1016/j.ssc.2009.12.038>
- Morris, J. R., Wang, C. Z., Ho, K. M., & Chan, C. T. (1994). Melting line of aluminum from simulations of coexisting phases. *Physical Review B*, 49(5), 3109–3115. <https://doi.org/10.1103/physrevb.49.3109>
- Mosenfelder, J. L., Asimow, P. D., Frost, D. J., Rubie, D. C., & Ahrens, T. J. (2009). The  $\text{MgSiO}_3$  system at high pressure: Thermodynamic properties of perovskite, postperovskite, and melt from global inversion of shock and static compression data. *Journal of Geophysical Research*, 114(B1), B01203. <https://doi.org/10.1029/2008jb005900>
- Nomura, R., Zhou, Y., & Irifune, T. (2017). Melting phase relations in the  $\text{MgSiO}_3\text{-CaSiO}_3$  system at 24 GPa. *Progress in Earth and Planetary Science*, 4(1), 34. <https://doi.org/10.1186/s40645-017-0149-2>
- Ohnishi, S., Kuwayama, Y., & Inoue, T. (2017). Melting relations in the  $\text{MgO-MgSiO}_3$  sSnmmyo, R., Tateno, S. (2018). Ystem up to 70 GPa. *Physics and Chemistry of Minerals*, 44(6), 445–453. <https://doi.org/10.1007/s00269-017-0871-8>
- Ozawa, K., Anzai, M., Hirose, K., Sinmyo, R., & Tateno, S. (2018). Experimental determination of eutectic liquid compositions in the  $\text{MgO-SiO}_2$  system to the lowermost mantle pressures. *Geophysical Research Letters*, 45(18), 9552–9558. <https://doi.org/10.1029/2018gl079313>
- Pradhan, G. K., Fiquet, G., Siebert, J., Auzende, A. L., Morard, G., Antonangeli, D., & Garbarino, G. (2015). Melting of MORB at core-mantle boundary. *Earth and Planetary Science Letters*, 431, 247–255. <https://doi.org/10.1016/j.epsl.2015.09.034>

- Richet, P., Robie, R. A., & Hemingway, B. S. (1991). Thermodynamic properties of wollastonite, pseudowollastonite and  $\text{CaSiO}_3$  glass and liquid. *European Journal of Mineralogy*, 3(3), 475–484. <https://doi.org/10.1127/ejm/3/3/0475>
- Shen, G., & Lazor, P. (1995). Measurement of melting temperatures of some minerals under lower mantle pressures. *Journal of Geophysical Research*, 100(B9), 17699–17713. <https://doi.org/10.1029/95jb01864>
- Soubiran, F., & Militzer, B. (2020). Anharmonicity and phase diagram of magnesium oxide in the megabar regime. *Physical Review Letters*, 125(17), 175701. <https://doi.org/10.1103/physrevlett.125.175701>
- Stixrude, L., & Lithgow-Bertelloni, C. (2012). Geophysics of chemical heterogeneity in the mantle. *Annual Review of Earth and Planetary Sciences*, 40(1), 569–595. <https://doi.org/10.1146/annurev.earth.36.031207.124244>
- Tateno, S., Hirose, K., Sakata, S., Yonemitsu, K., Ozawa, H., Hirata, T., et al. (2018). Melting phase relations and element partitioning in MORB to lowermost mantle conditions. *Journal of Geophysical Research: Solid Earth*, 123(7), 5515–5531. <https://doi.org/10.1029/2018jb015790>
- Trønnes, R. G., Baron, M. A., Eigenmann, K. R., Guren, M. G., Heyn, B. H., Løken, A., & Mohn, C. E. (2019). Core formation, mantle differentiation and core-mantle interaction within Earth and the terrestrial planets. *Tectonophysics*, 760, 165–198. <https://doi.org/10.1016/j.tecto.2018.10.021>
- Trønnes, R. G., Mohn, C. E., Grømer, B., Hernandez, J.-A., Guren, M. G., & Baron, M. A. (2021). High-density residual Ca-perovskite in the lowermost mantle. *Abstr., Collaborative study of Earth's core-mantle boundary region, Roy. Astr. Soc., UK-SEDI, Nov., 12, 2021*.
- Tschauner, O., Huang, S., Yang, S., Humayun, M., Liu, W., Gilbert Corder, S. N., et al. (2021). Discovery of davemaoite,  $\text{CaSiO}_3$ -perovskite, as a mineral from the lower mantle. *Science*, 374(6593), 891. <https://doi.org/10.1126/science.abo2029>
- Tsuchiya, T., & Tsuchiya, J. (2011). Prediction of a hexagonal  $\text{SiO}_2$  phase affecting stabilities of  $\text{MgSiO}_3$  and  $\text{CaSiO}_3$  at multimegabar pressures. *Proceedings of the National Academy of Sciences*, 108(4), 1252–1255. <https://doi.org/10.1073/pnas.1013594108>
- von Simon, F., & Glatzel, G. (1929). Bernerkungen zur Schmelzdruckkurve. *Zeitschrift für Anorganische und Allgemeine Chemie*, 178(1), 309–316. <https://doi.org/10.1002/zaac.19291780123>
- Walter, M. J., Kohn, S. C., Araujo, D., Bulanova, G. P., Smith, C. B., Gaillou, E., et al. (2011). Deep mantle cycling of oceanic crust: Evidence from diamonds and their mineral inclusions. *Science*, 334(6052), 54–57. <https://doi.org/10.1126/science.1209300>
- Walter, M. J., Kohn, S. C., Pearson, D. G., Shirey, S. B., Speich, L., Stachel, T., et al. (2022). Comment on “Discovery of davemaoite,  $\text{CaSiO}_3$ -perovskite, as a mineral from the lower mantle”. *Science*, 376(6593). <https://doi.org/10.1126/science.abo0882>
- Walter, M. J., Thomson, A. R., & Smith, E. (2022). Geochemistry of silicate and oxide inclusions in sublithospheric diamonds. *Reviews in Mineralogy and Geochemistry*, 88(1), 393–450. <https://doi.org/10.2138/rmg.2022.88.07>
- Wentzcovitch, R. M., Martins, J. L., & Allen, P. B. (1992). Energy versus free-energy conservation in first-principles molecular dynamics. *Physical Review B*, 45(19), 11372–11374. <https://doi.org/10.1103/physrevb.45.11372>
- White, W. M. (2015). Isotopes, DUPAL, LLSVPs, and anakavada. *Chemical Geology*, 419, 10–28. <https://doi.org/10.1016/j.chemgeo.2015.09.026>
- Wilson, A., & Stixrude, L. (2021). Entropy, freezing and dynamics of  $\text{CaSiO}_3$  liquid. *Geochemical et Cosmochemica Acta*, 302, 1–17. <https://doi.org/10.1016/j.gca.2021.03.015>
- Yao, J., Frost, D. J., & Steinle-Neumann, G. (2021). Lower mantle melting: Experiments and thermodynamic modelling in the system  $\text{MgO-SiO}_2$ . *Journal of Geophysical Research*, 126, e2021JB022568.
- Yuan, L., & Steinle-Neumann, G. (2020). Strong sequestration of hydrogen into the Earth's core during planetary differentiation. *Geophysical Research Letters*, 47(15), e2020GL088303. <https://doi.org/10.1029/2020gl088303>
- Zerr, A., Serghiu, G., & Boehler, R. (1997). Melting of  $\text{CaSiO}_3$  perovskite to 430 kbar and first in-situ. *Geophysical Research Letters*, 24(8), 909–912. <https://doi.org/10.1029/97gl00829>
- Zhu, L.-F., Körmann, F., Ruban, A. V., Neugebauer, J., & Grabowski, B. (2020). Performance of the standard exchange-correlation functionals in predicting melting properties fully from first principles: Application to al and magnetic ni. *Physical Review B: Condensed Matter*, 101(14), 144108. <https://doi.org/10.1103/physrevb.101.144108>

## References From the Supporting Information

- Alfè, D., Cazorla, C., & Gillan, M. J. (2011). The kinetics of homogeneous melting beyond the limit of superheating. *Journal of Chemical Physics*, 135(2), 024102. <https://doi.org/10.1063/1.3605601>
- Baldereschi, A. (1973). Mean-value point in the Brillouin zone. *Physical Review B*, 7(12), 5212–5215. <https://doi.org/10.1103/physrevb.7.5212>
- Berens, P. H., Mackay, D. H., White, G. M., & Wilson, K. R. (1983). Thermodynamics and quantum corrections from molecular dynamics for liquid water. *Journal of Chemical Physics*, 79(5), 2375–2389. <https://doi.org/10.1063/1.446044>
- Bernhardt, M. (2016). *Solvation thermodynamic properties from molecular dynamics on the terahertz time scale* Master's thesis, Technische Universität.
- Blöch, P. E. (1994). Projector augmented-wave method. *Physical Review B*, 50(24), 17953–17979. <https://doi.org/10.1103/physrevb.50.17953>
- Irifune, T., Miyashita, M., Inoue, T., Ando, J., Funakoshi, K., & Utsumi, W. (2000). High-pressure phase transformation in  $\text{CaMgSi}_2\text{O}_6$  and implications for origin of ultra-deep diamond inclusions. *Geophysical Research Letters*, 27(21), 3541–3544. <https://doi.org/10.1029/2000gl012105>
- Jung, D. Y., & Schmidt, M. W. (2011). Solid solution behavior of  $\text{CaSiO}_3$  and  $\text{MgSiO}_3$  perovskites. *Physics and Chemistry of Minerals*, 38(4), 311–319. <https://doi.org/10.1007/s00269-010-0405-0>
- Kresse, G., & Hafner, J. (1994). Ab initio molecular-dynamics simulation of the liquid-metal-amorphous-semiconductor transition in germanium. *Physical Review B*, 49(20), 14251–14269. <https://doi.org/10.1103/physrevb.49.14251>
- Kresse, G., & Joubert, D. (1999). From ultrasoft pseudopotentials to the projector augmented-wave method. *Physical Review B*, 59, 3–4. <https://doi.org/10.1103/physrevb.59.1758>
- Kuwayama, Y., Hirose, K., Cobden, L., Kusakabe, M., Tateno, S., & Ohishi, Y. (2022). Post-perovskite phase transition in the pyrolytic lowermost mantle: Implications for ubiquitous occurrence of post-perovskite above CMB. *Geophysical Research Letters*, 49(1), e2021GL096219. <https://doi.org/10.1029/2021gl096219>
- Mermin, N. D. (1965). Thermal properties of the inhomogeneous electron gas. *Physics Review*, 137(5A), A1441–A1443. <https://doi.org/10.1103/physrev.137.a1441>
- Muir, J. M. R., Thomson, A. R., & Zhang, F. (2021). The miscibility of calcium silicate perovskite and bridgmanite: A single perovskite solid solution in hot, iron-rich regions. *Earth and Planetary Science Letters*, 566, 116973. <https://doi.org/10.1016/j.epsl.2021.116973>
- Perdew, J. P., Burke, K., & Ernzerhof, M. (1996). Generalized gradient approximation made simple. *Physical Review Letters*, 77(18), 3865–3868. <https://doi.org/10.1103/physrevlett.77.3865>

# Supporting Information for

## ***Ab initio* atomistic simulations of Ca-perovskite melting**

**J.-A. Hernandez<sup>1,2</sup>, C.E. Mohn<sup>1</sup>, M. G. Guren<sup>1,3</sup>, M. A. Baron<sup>1,4</sup>, R. G. Trønnnes<sup>1,5</sup>**

<sup>1</sup>Centre for Earth Evolution and Dynamics, University of Oslo, Norway.

<sup>2</sup>Currently: European Synchrotron Radiation Facility, Grenoble, France.

<sup>3</sup>Currently: Njord Centre, Department of Geoscience, University of Oslo, Norway.

<sup>4</sup>Currently: Laboratoire de Chimie de la Matière Condensée de Paris, UMR 7574, Sorbonne Université, CNRS, Collège de France.

<sup>5</sup>Natural History Museum, University of Oslo, Norway.

### **Contents of this file**

Text S1 to S3

Figures S1 to S8

Table S1 to S2

Excel files: *2PT.xlsx* and *TI.xlsx* are provided at <https://osf.io/982vn>

### **Text S1. Methods**

#### Details on the 2PT approach

In the 2PT approach we decomposed the Gibbs free energy of a given phase as follows:

$$g = u_{MD} + u_{qc} + pV - T(s_{el} + s_{ion}) \quad (1)$$

where  $u_{MD}$ ,  $u_{qc}$ ,  $p$ ,  $V$ ,  $T$ ,  $s_{el}$  and  $s_{ion}$  are the internal energy from the DFT-MD, an energy correction for the nuclear quantum effects (NQE), the pressure, volume, temperature, and electronic and ionic entropies of the system, respectively. The use of small letters for the internal energy and the entropy indicate the energy per mass unit. At given  $V$  and  $T$ , the internal energy ( $u_{MD}$ ), electronic entropy ( $s_{el}$ ) and temperature are straightforwardly obtained from the DFT-MD. The ionic entropy ( $s_{ion}$ ), assumed to be equal to the vibrational entropy, and the correction to the internal energy ( $u_{qc}$ ) for NQE, are determined based on partial vibrational power spectra obtained from the atomic trajectories. In the case of the solid, both  $u_{qc}$  and  $s_{vib}$  are obtained by a weighted integration of the vibrational power spectra, considering a quantum harmonic oscillator (QHO) model for  $s_{ion}$ , and from both a QHO and classical harmonic oscillator model for  $u_{qc}$  (e.g. Berens et al. 1983). In the liquid case, we use the two-phase thermodynamic model (2PT-MF; Lin et al., 2003) as modified by Desjarlais (Desjarlais, 2013), which decomposes the partial vibrational power spectra into a gas-like (diffusive) and a solid-like (vibrational) component. The gas-like component is modelled as the gas component of a hard-sphere fluid and is fitted to the zero-frequency intensity of the partial vibrational spectrum and to its high-frequency tail. For each atom type, the partial molar volume is approximated for each atom type by the volume of a sphere with the corresponding Wigner-Seitz radius. The solid-like part is obtained by subtracting the gas-like component from the partial vibrational spectrum and treated as a QHO. This decomposition is done for each atomic species present in the simulation, and  $u_{qc}$  and  $s_{ion}$  are obtained by the recombination of the partial molar internal energies ( $\bar{U}_i$ ) and entropies ( $\bar{S}_i$ ) obtained from the vibrational power spectrum of a given species  $i$ :

$$u_{qc} = \frac{\sum_i N_i}{\sum_i m_i N_i} \sum_i x_i \bar{U}_i - u_{MD} \quad (2)$$

$$s_{ion} = \frac{\sum_i N_i}{\sum_i m_i N_i} \sum_i x_i \bar{S}_i + s_{mix} \quad (3)$$

where  $x_i$ ,  $N_i$  and  $m_i$  are molar fractions, number of atoms and atomic mass of a given species  $i$ , respectively.  $s_{mix}$  is a mixing term controlling the compositional dependence. In the solid phase,  $s_{mix} = 0$  because the atoms are considered distinguishable, and only perfect crystals are considered here. In the derivation of the 2PT model for multicomponent atomic liquids (Lai et al., 2012; Bernhardt, 2016),  $s_{mix}$  is an ideal mixing term ( $s_{mix} = -k \frac{\sum_i N_i}{\sum_i m_i N_i} \sum_i x_i \ln x_i$ ) which ensures that the mixing entropy equals the ideal mixture if the different species present similar vibrational spectra. In principle, the pressure should also be corrected for NQE, but

this correction is negligible due to the high-temperature conditions of this study and the absence of light elements such as H.

### Computational details

All calculations were performed using the Vienna *ab-initio* simulation package (VASP 5.2; e.g. Kresse and Hafner, 1994) using the DFT GGA functional to calculate the exchange-correlation contribution to the total energy. The projector augmented-wave (PAW) method (Blöchl, 1994; Kresse and Joubert, 1999) was used together with the Perdew-Burke-Ernzerhof (PBE, Perdew et al., 1996) functional. The valence electron configuration was  $2s^2 2p^4$  for O,  $3s^2 3p^2$  for Si and  $3s^2 3p^6 4s^2$  for Ca. A cut-off energy of 400 eV for the plane waves were used in the large-cell and small-cell coexisting calculations, whereas an energy cutoff of 900 eV were used in the “free energy” (TI and 2PT) calculations. Such a high cutoff is required for the accurate calculations of absolute free energies. Less accuracy is required in the two-phase calculations since there is no need to calculate the absolute free energy. With a cutoff of 900 eV for the plane wave expansion and a calculation done at the Baldereschi point, internal energy and pressure are converge to within  $5 \times 10^{-4}$  eV/at and 0.05 GPa compared to a simulation with 2000 eV cutoff and  $2 \times 2 \times 2$  k-point grid. The chosen cutoff ensures that the electronic structure and stress are computed accurately enough to represent a negligible source of error compared to those resulting from time-averaged statistics and the chosen free energy calculation scheme. Also, it still allows us to run long MD simulations compare to a larger cutoff energy or denser k-point grid. In the 120-atom two-phase simulations at 120 GPa, we investigated the sensitivity of melting pressure to the choice of energy cutoff and found that the average pressure increased by less than 4 GPa when increasing the energy cutoff systematically from 400 to 600 eV. In all calculations the electronic entropy was included using a Fermi-Dirac smearing with a width of  $k_B T$  (Mermin, 1965).

The large-cell solid-melt coexistence calculations were carried out using 720-atom cells, whereas in the small-cell calculations we used 80-, 120- and 240-atom cells with a Brillouin zone sampling containing the  $\Gamma$ -point only. The large-cell calculations ran for between 12 and 168 ps, whereas the small-cell calculations typically ended in a single phase within 10 ps, although some ran for more than 20 ps before collapsing into a single phase.

The large-cell solid-melt coexistence molecular dynamics calculations were carried out in the *NVT* ensemble using a Nosé-*Hoover* thermostat with a time step of 1 or 2 fs. The small-cell coexistence simulations ran in the *NPT* ensemble, using Nosé-*Hoover* thermo- and barostats with a time step of 1 fs, as implemented SLUSCHI (Hong and Van De Walle, 2016). Use of *NPT* is often advantageous for direct verification of experimental results and avoids non-hydrostatic conditions during equilibration (Belonshko, 1994). However, we do not expect that possible non-hydrostatic conditions in the large-cell solid-melt coexistence *NVT* runs will influence the melting of Ca-perovskite, which is cubic close to the melting temperature.

Most MD runs for the free energy calculations were also carried out in the *NVT* ensemble with a Nosé-*Hoover* thermostat and a time steps of 1 fs, except for the TI calculations with  $\lambda$ -values  $< 10^{-2}$  where a Langevin thermostat and smaller time steps of 0.5 or 0.25 fs are needed. In order to converge the power spectra and thermodynamic properties (to within  $\sim 0.1$  kJ/g) in the 2PT calculations of the liquid free energy, long trajectories of 10 to 65 ps were acquired.

The TI and 2PT free energy calculations for liquids were carried out at the  $\Gamma$ -point in  $4 \times 4 \times 4$  (320 atoms) supercell and at the Baldereschi mean-value point (Baldereschi 1973) in Ca-perovskite, using a  $3 \times 3 \times 3$  (135-atom) supercell. Use of Baldereschi point lowers the computational cost and is as accurate as a denser  $2 \times 2 \times 2$  k-points (Monkhorst-Pack) grid.

In the 2PT approach, the ionic entropy ( $s_{\text{ion}}$ ) was computed by a weighted integral of the vibrational spectrum. The low frequency part is strongly weighted and corresponds to long wavelength vibrational modes, whose sampling depends on the size of the supercell used in the MD runs. We also found a more modest cell-size dependence of electronic entropy ( $s_{\text{el}}$ ) and the  $u+pV$  term. Therefore, we critically examined cell-size effects by computing the evolution of the thermodynamic quantities with  $2 \times 2 \times 2$  and  $4 \times 4 \times 4$  supercells (containing 40 and 320 atoms respectively) and extrapolated their values to infinite cell-size (Figure S3). The ionic entropy energy term is by far the most sensitive to the cell-size.

For the TI approach in the liquid,  $\langle U_{DFT} \rangle_\lambda$  was evaluated at 7  $\lambda$ -points (6  $\lambda$ -values between 0.003 and 1 plus  $\lambda = 0$  that is constrained by the change of variable used for the integration). We were not able to successfully run simulations with smaller  $\lambda$ -values as the atoms come too close to each other for the electronic wave function to converge. A polynomial expression was then fitted to the data points prior to integration over  $x$ . Integration paths are shown in Figure S4.



The supplementary files *2PT.xlsx* and *TI.xlsx* (provided at <https://osf.io/982vn>) summarise all the relevant data for the 2PT and TI approaches. The corresponding Gibbs free energy curves are shown in Figure S5, and the resulting melting points are collected in Table S1 together with results from large-cell and small-cell solid-melt coexistence methods. Figure S6 shows the evolution of pressure and  $Ts$  terms as function of density and compares our entropy estimates to previous DFT (Wilson and Stixrude, 2021) and experimental data (Richet et al., 1991).

Preparation of solid-liquid boundaries in the two-phase calculations is a crucial step in order to avoid lengthy equilibration times due to “ill defined” or “unphysical” initial configurations. In the large-cell solid-melt coexistence method, the 720-atoms simulation box was prepared from two cubic  $4\times 4\times 4$  sub-cells (containing 360 atoms each), which were heated and equilibrated at the target temperatures. The configuration representing the liquid was constructed by first heating to a very high temperature (about 11000 K) before cooling to the target temperature. The initial supercell, containing both phases, was then constructed by merging the two sub-cells, leaving a very small “empty space” ( $< 0.5$  Å) in between the configurations to avoid too short interatomic distances (Di Paola and Brodholt, 2016). Many of these large-cell solid-melt coexistence runs were not started from “scratch” by equilibrating and gluing separate boxes with solid and liquids, but were restarted with new forces from configurations used in previous simulations where solid-liquid interfaces were equilibrated or intact.

For the small-cell solid-melt coexistence calculations, we follow a similar procedure, but since the melting temperature is much more sensitive to the nature of the boundary, we prepared the boundary as described by Alfè (2005) and constructed supercells as implemented in SLUSCHI (Hong and Van De Walle, 2016). After launching an MD run in a simulation box, a plane defining the boundary was identified. Half of the box was then kept frozen, while the other half was heated further until melting. Finally, the liquid part is cooled down to the desired temperature. This procedure ensures that the chemical bonds at the interfaces are physically reasonable. To minimize interaction among images of the supercell due to periodic boundary conditions, the cell shape was chosen to have dimensions  $2a\times a\times a$  with angles  $60^\circ$ ,  $90^\circ$  and  $90^\circ$ , where  $a$  is a parameter defining the size of the simulation box. The small-cell simulations were performed using the small-size solid-melt coexistence method (see Figure S2), run in the  $NPT$  ensemble using Nosé-Hoover thermo- and barostats (Hong and Van De Walle, 2016). Based on the molecular dynamics simulations at each of the four pressures, the corresponding melting points were calculated from the fitting procedure shown in Figure S7.

## Text S2. Calculation of homogenous and equilibrium melting temperatures using the Z method

To calculate the melting temperature using the Z method, a number of MD simulations were carried out at different energies,  $E$ , in the microcanonical ( $NVE$ ) ensemble to target the homogeneous melting temperature,  $T_h$ . From  $T_h$  we estimated the equilibrium melting temperature,  $T_m$ , as the lowest temperature at the isochore with energy  $E_h$ . As the solid eventually melts at a constant  $E = E_h$ , the temperature drops when kinetic energy is converted to potential energy. Note that in *ab initio* MD simulations in the microcanonical ensemble, the conserved quantity is  $E_K + U - TS^{\text{el}}$ , where  $E_K$  is the kinetic energy of the ions,  $U$  is the DFT energy and  $S^{\text{el}}$  is the electronic entropy (Mermin, 1995; Wentzcowitch et al. 1992). The electronic entropy can be calculated from the Fermi-Dirac (FD) distribution of the occupancies of the different states and  $U$  will therefore be affected by the choice of the FD “smearing” parameter,  $\sigma$ , in the canonical ensemble. If two MD runs are launched with different values of  $\sigma$ , but with the same kinetic and potential energy, the total energy will be more negative in the run with higher electronic entropy. This, in turn can influence the homogeneous melting temperature. To avoid bias on  $T_h$  in the choice of initial parameters we explored different strategies in targeting the homogeneous melting temperature. In one of these we launched a sequence of short MD simulations (each  $\sim 1$  ps) and restarted at run  $i + 1$  with  $\sigma$  updated to match the average temperature in the previous MD run  $i$ . This means that  $\sigma_{i+1} = k_B \langle T_i \rangle$ . After self-consistency with  $\langle T_i \rangle = \langle T_{i+1} \rangle$ , the melting temperature is not affected by the choice of initial conditions. This implementation ensures that  $E_K + U - TS^{\text{el}}$  is conserved (Wentzcowitch et al., 1992). In a different strategy, we carried out several MD simulations with different values of  $\sigma$  to find the “optimal” value where the average temperature equals  $T_h$ .

Our Z-method calculations were performed at a volume of  $4.91 \text{ cm}^3/\text{mol/atom}$  within a 135-atom simulation box with all the atoms initially located at their equilibrium lattice-positions in the crystal structure. The energy cut-off was 500 eV, the functional was PBEsol, we used the Ca PAW pseudopotential with 10 valence electrons, and only the gamma-point was included to sample the first Brillouin zone. These settings are the same as those used in Braithwaite and Stixrude (2019). To compare with our melting curves reported in Figure 1, we also calculated  $T_m$  using the PBE functional and the Ca PAW pseudopotential with 8 valence electrons. In addition, we performed Z-method simulations where the FD smearing was *kept fixed* at  $\sigma/k_B = 9000 \text{ K}$  along the entire MD trajectory, as discussed above. This temperature corresponds roughly to the  $T_h$  found in the simulation where the FD smearing is updated along the trajectory.



Table S2 shows that the calculated homogeneous melting temperature is more than 1500 K higher than that reported by Braithwaite and Stixrude (2019). An MD run with  $\sigma/k_B$  kept fixed at 9000 K along the trajectory, shows no evidence for melting even after more than 50 ps (see Figure S8), providing strong evidence for a high homogeneous melting temperature. The average temperature from this run is very close to the  $T_h$  estimated from a fit along the solid branch in the  $E, T$  space, which is only slightly higher than the estimated homogeneous melting temperature of 8720 K. Therefore, the average temperature from the run with  $\sigma/k_B = 9000$  K probably represents a strict *lower bound* to  $T_h$ . The discrepancy between our calculated  $T_h$  and that of Braithwaite and Stixrude (2019) could thus possibly result from the choice of the Fermi-Dirac smearing parameter, since a high value of FD smearing would result in a premature melting, a low homogeneous melting temperature and hence a low  $T_m$ .

Braithwaite and Stixrude (2019) calculated the melting temperature using a waiting time analysis but did not report the contribution from the waiting time,  $\tau_w$ , to the reported melting temperature. To compare directly with that of Braithwaite and Stixrude (2019), we therefore need to calculate the contribution to the melting temperature from the waiting time to melt. We calculated the time it takes for a solid to melt at a temperature  $T_l$  in a number of MD simulations where  $E > E_h$ . We then used a similar relation as that of Braithwaite and Stixrude (2019), proposed by Alf   et al. (2011):  $\tau_w^{-1/2} = A(T_l - T_m)$ . The equilibrium melting temperature is then obtained as the intercept of this relation at  $\tau_w^{-1/2} = 0$ . Using the PBEsol functional, we find that the resulting melting temperature at 105.5 GPa is 6493 K (Table S2). This is in very good agreement with our melting curves shown in Fig. 1, and with that calculated using PBE.

### Text S3. Ca-perovskite composition in basaltic and peridotitic rocks and diamond inclusions

The composition of Ca-perovskite in peridotitic and basaltic lithologies, as well as in diamond inclusions, is close to  $\text{CaSiO}_3$ , and each of the minor elements, Ti, Al, Fe, Mg and Na are mostly present in concentrations below 2 cation% (e.g. Corgne et al. 2005; Tateno et al., 2018; Walter et al. 2022b). The small grain size of subsolidus Ca-perovskite challenges the microanalytical accuracy, such that fluorescent X-ray generation in neighbouring grains will tend to give too high concentrations of elements like Mg, Fe and Al and too low concentrations of elements like Ca and Ti. Although the melting experiment of Tateno et al. (2018) yielded increasing cpv/melt partition coefficients for Na and K (measured by EMPA) with increasing pressure in the 32-135 GPa range, the contents of Na and K in Ca-perovskite do not exceed 1.0 and 0.3 atom% (or 2.5 and 0.7 cation%), respectively, even at 135 GPa.

Along the  $\text{MgSiO}_3$ - $\text{CaSiO}_3$  join at 24 GPa and 2500 K, the experiments by Nomura et al. (2017), combined with the Irifune et al. (2000) results, indicate that the immiscibility gap between bridgmanite and Ca-perovskite covers the 3-88 mol%  $\text{CaSiO}_3$  range. This is narrower than the 2-98 mol% gap of Jung and Schmidt (2011), based on ab initio simulations. The more extensive solid solution range, especially of Ca-perovskite in fine-grained subsolidus to solidus products might partly be due some X-ray fluorescence contributions from neighbouring grains during EMPA analysis. The ab initio results of Muir et al. (2021) imply very restricted solid solutions at similar p-T conditions. However, they record an abrupt transition to complete solid solution above 3170, 3050 and 2740 K at 25, 75 and 125 GPa, respectively, which contradicts all experimental data at suprasolidus conditions at pressures exceeding about 80 GPa (e.g. Pradhan et al., 2015; Tateno et al., 2018; Kuwayama et al., 2021). The basaltic inclusion suite (except for stishovite) in diamonds from the Juina-5 kimberlite (Walter et al. 2011) corresponds to the experimental results on basaltic compositions. The compositional Ca-perovskite range is limited, and Na, and in particular K, are low for both Juina inclusions and the experimental products on basaltic compositions. These analytical results are supported by a larger database compiled and reported by Walter et al. (2022b).

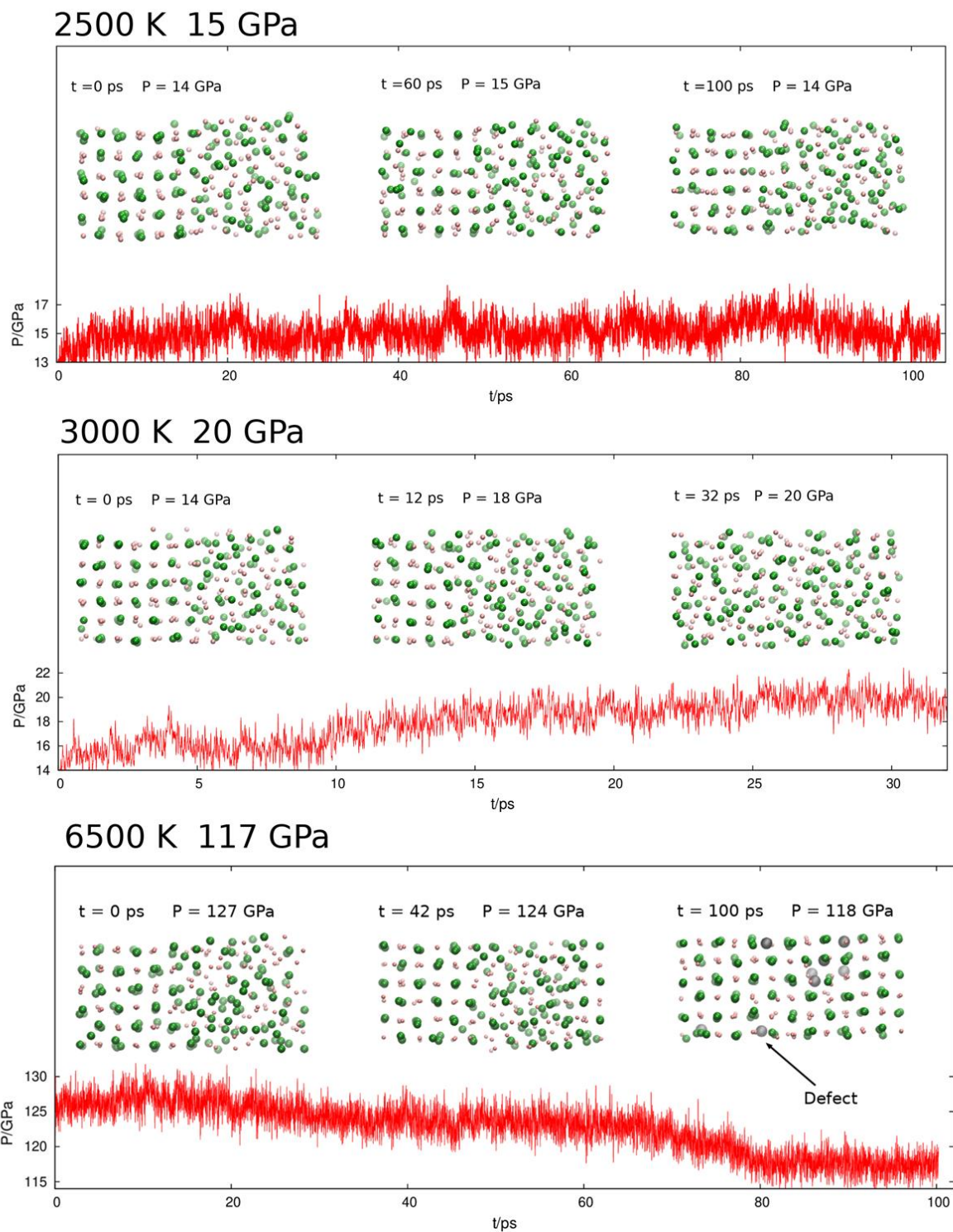


**Figure S1.** Changes in pressure along the trajectory in large-cell coexistence calculations. Three snapshots of the configurations are shown where large green spheres and small light brown spheres represent the calcium and silicon ions respectively. The oxygens are removed for clarity. Top figure shows an example where a solid-liquid boundary is intact and still stable after more than 100 ps. Middle and bottom figures are runs that end up in a liquid or solid configuration, respectively, in less than 100 ps.

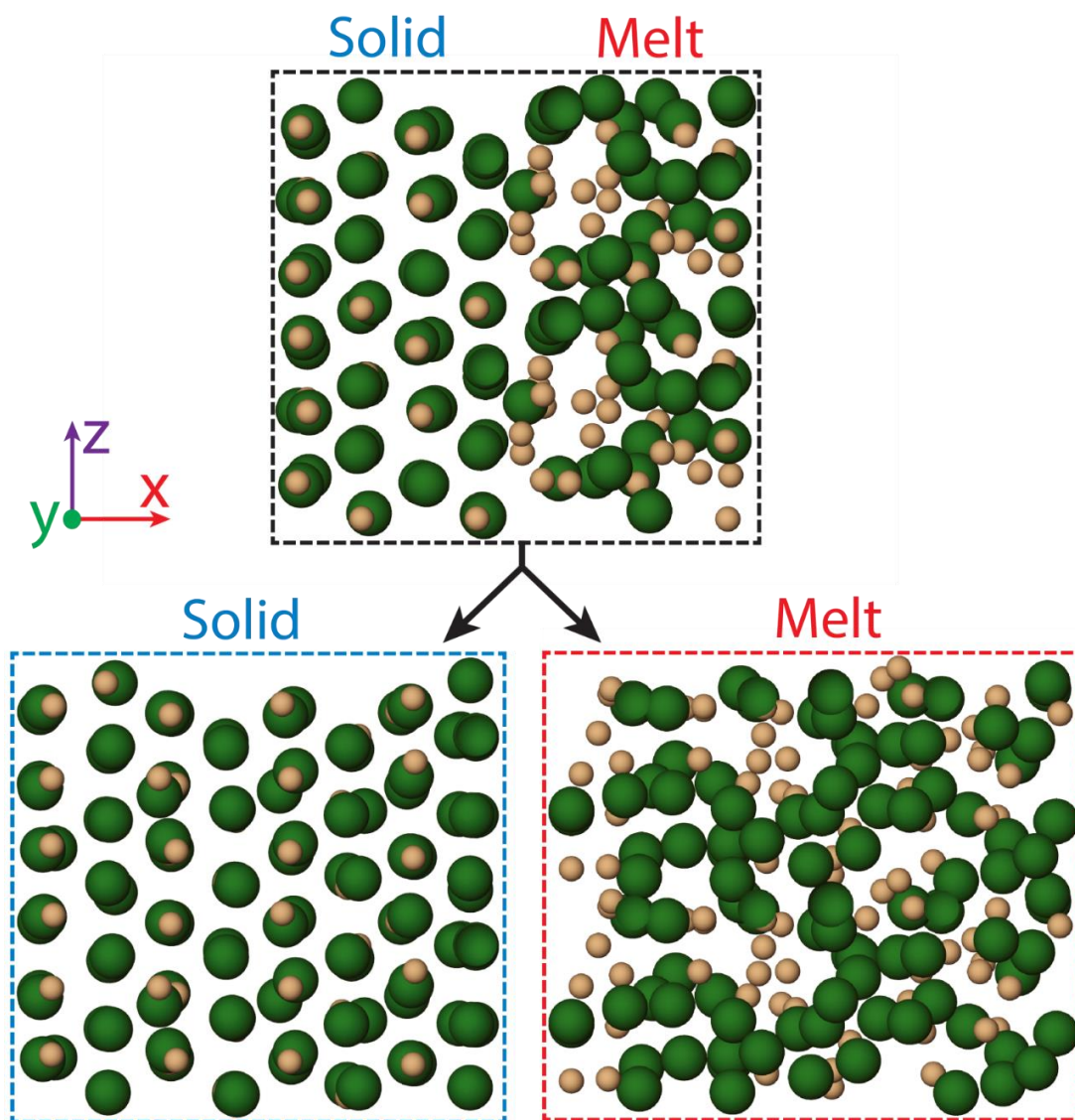


**Figure S2.** Snapshots of typical configurations from small-cell coexisting calculations shown as projections along the y-direction of Ca (green) and Si (light brown). Starting with a solid-liquid boundary (top) the MD run either ends up in a single phase: 100% solid (bottom left) or 100% melt (bottom right). The O-atoms are omitted for clarity.

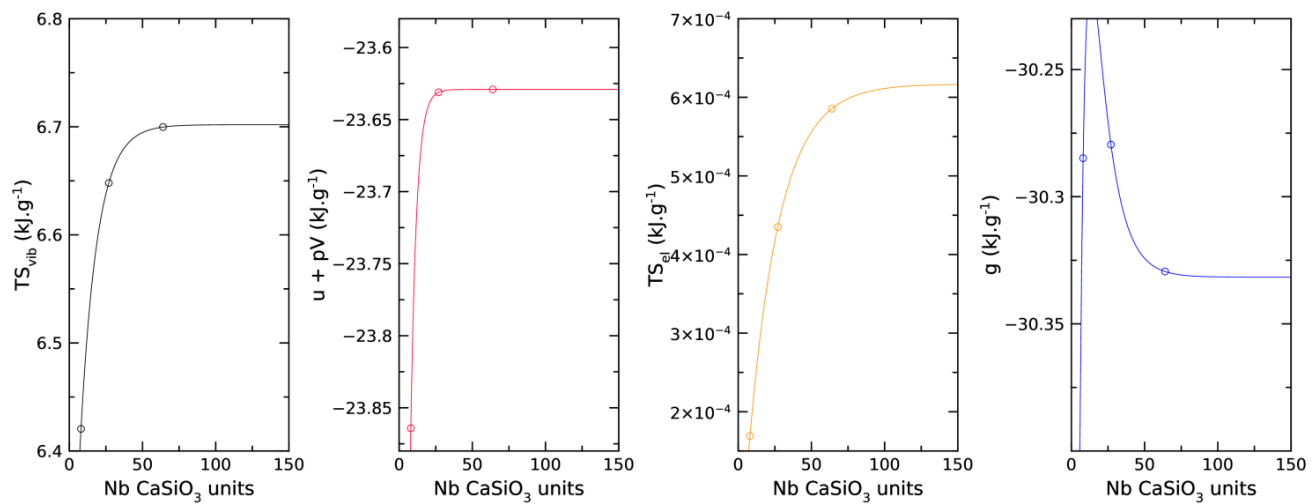


**Figure S3.** Cell size convergence of different component of the Gibbs free energy at 2500 K and ~15 GPa. The cell-size convergence of the different components of the Gibbs free energy is fitted by exponential functions.

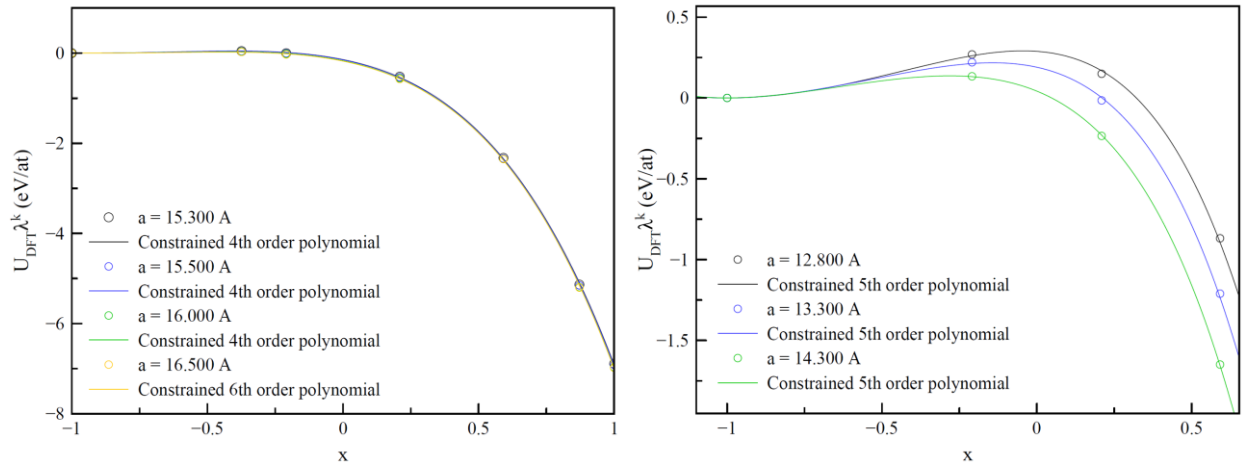


**Figure S4.** Integration paths at 2500 K (left) and 6000 K (right) and different volumes in the liquid phase. Circles and lines indicate the computed values and the polynomial fits used for numerical integration respectively. The parameter  $a$  corresponds to the length of the cubic supercell. Polynomial fits are constrained to have a zero slope and a convex curvature at  $x=0$ . Such constraints are consistent with the shape the integration path between the ideal gas and the DFT liquid in our study, but also in Yuan and Steinle-Neumann (2020) in liquid  $\text{MgSiO}_3$  and Dorner et al. (2018) in liquid Si.



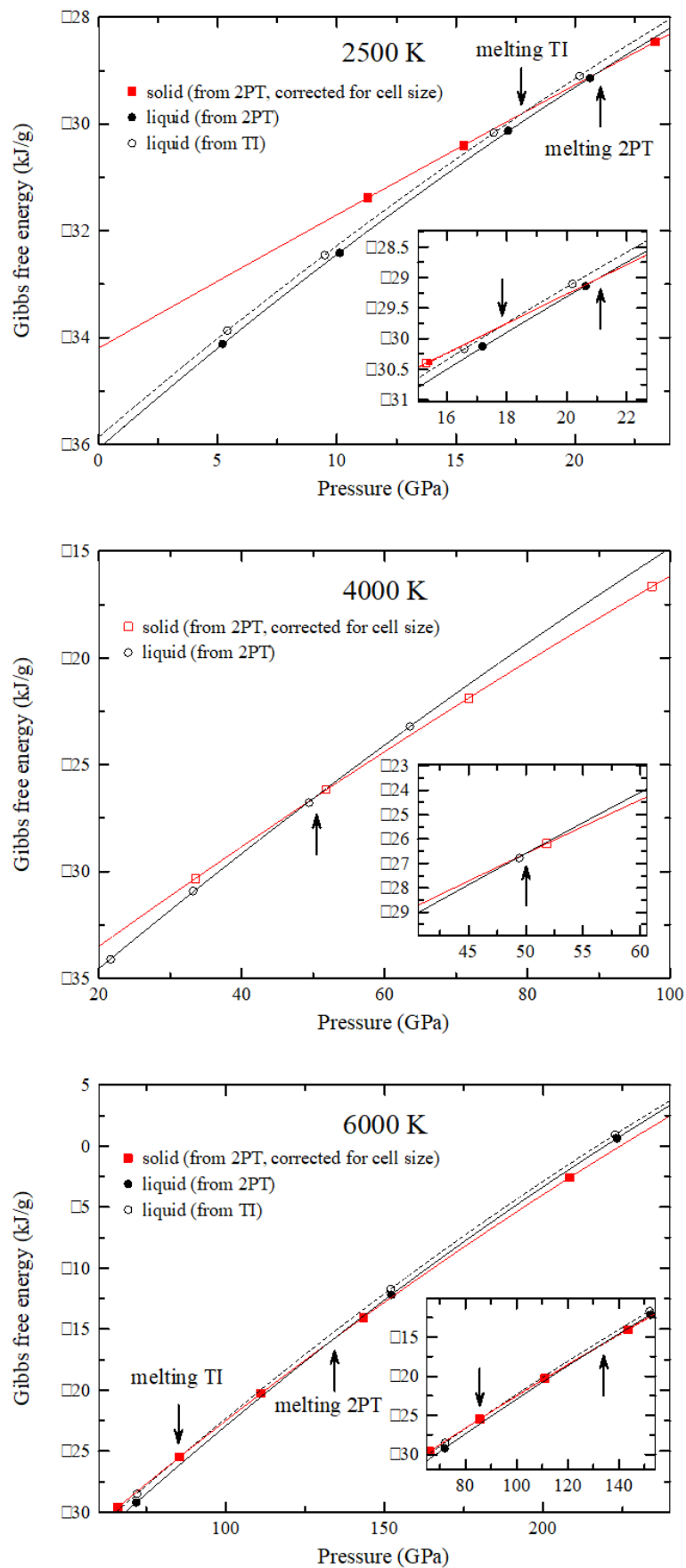


**Figure S5.** Gibbs free energy of CaSiO<sub>3</sub> Ca-perovskite and melt as function of pressure as obtained from both thermodynamic integration (TI) and 2PT approaches. The arrows indicate the melting conditions from each approach. Continuous and dashed lines are polynomial fit to 2PT and TI energies respectively.

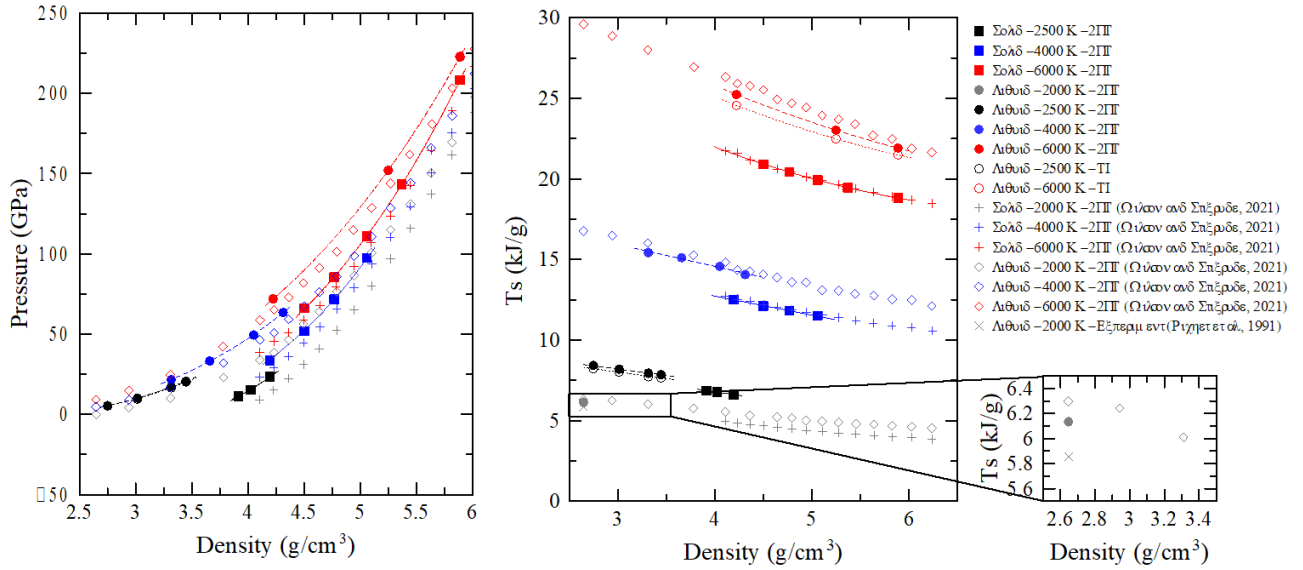


**Figure S6.** Left: Pressure-density relations obtained from our DFT-MD in  $\text{CaSiO}_3$  melt and Ca-perovskite at 2500 K, 4000 K and 6000 K. Solid lines correspond to third order Birch-Murnaghan equation of state fits of our Ca-perovskite data. Dashed and dotted lines are fits for our 2PT and TI liquid-state data, respectively. The derivative of the bulk modulus is fixed to 4 where 3 data points are present. The use of the PBE functional used in our study results in lower densities in both solid and liquid phases compared to the results reported in Wilson and Stixrude (2021) with PBEsol. However, at a given pressure, the relative density difference between the two phases remains similar for both functionals. Right:  $Ts$  is total entropy multiplied by temperature from the 2PT and TI approaches (ph. refers to the phonon calculations in the solid), compared with 2PT data points from Wilson and Stixrude (2021). While all approaches give the same entropy for Ca-perovskite within chemical accuracy (solid and open squares overlap), differences appear in the entropy of the melt. First, at fixed cell size and functional, our data show that the 2PT approach overestimates the entropy of the melt compared to TI, and compared to experimental data (see main text for more details and the comparison between computed data at 2000 K and Richet et al. (1991) measurements). Second, the 2PT data from Wilson and Stixrude (2021) gives higher values than ours with the same method, which is partly due to higher electronic entropies (possibly related to the use of different functionals) and to different system sizes. It is worth noting that when using the Wilson and Stixrude entropy data for the liquid state, we obtain a melting pressure of  $\sim 200$  GPa at 6000 K, in good agreement with their melting curve.

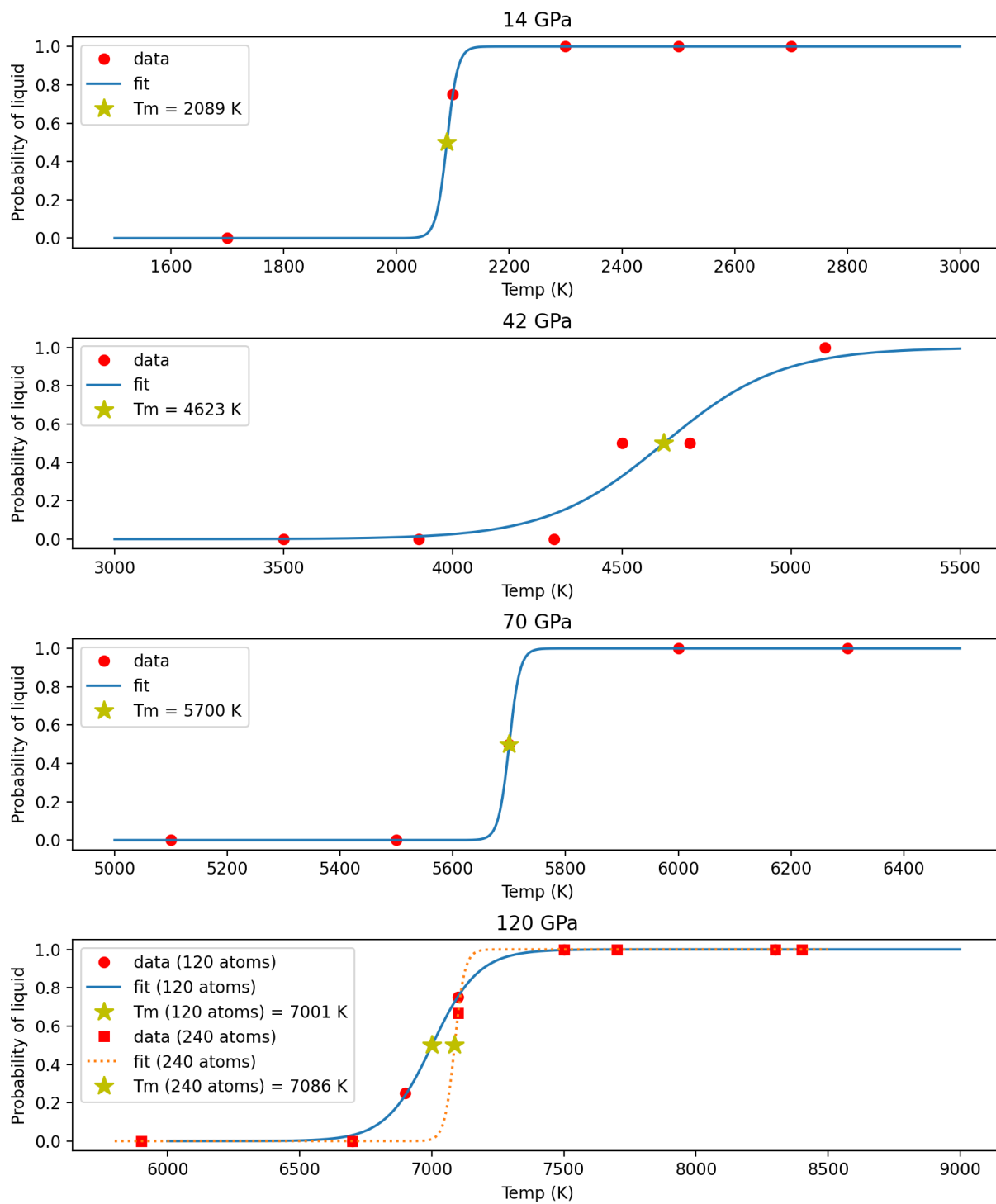


**Figure S7.** Distribution of trajectories that ends in a solid or liquid state. Melting temperatures are inferred from a fitting using a sigmoidal function of the statistical distributions. At each pressure we perform around 30 simulations.

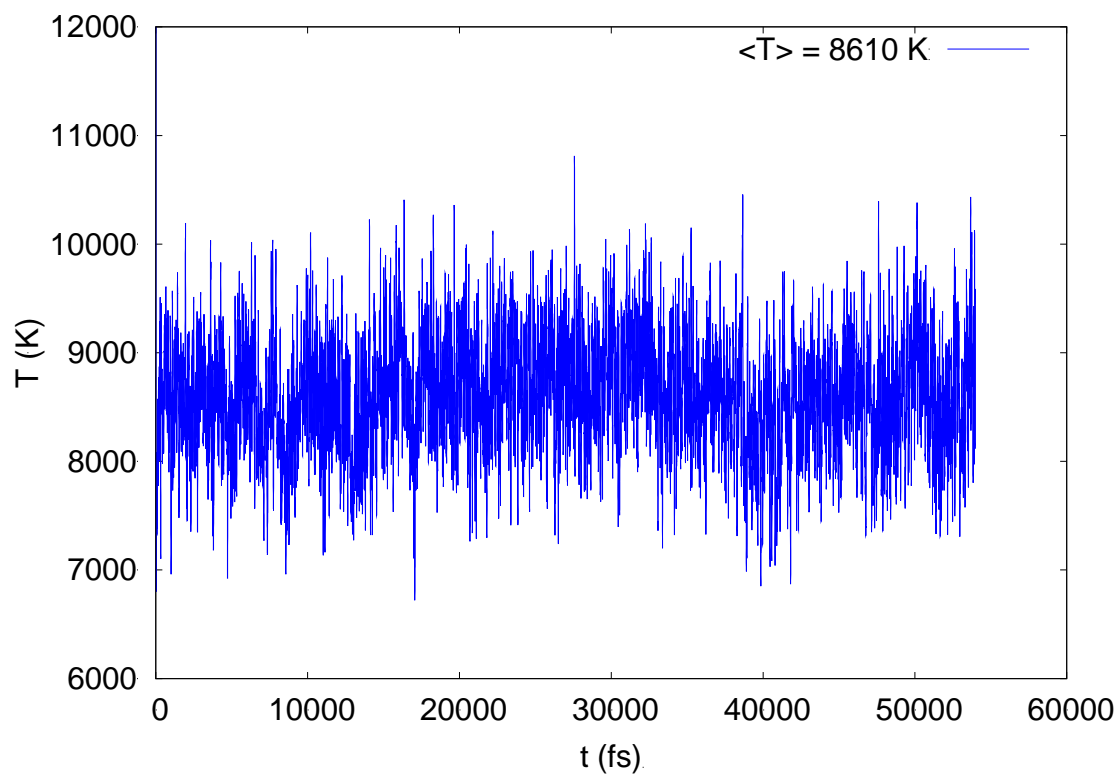


**Figure S8.** Temperature fluctuations in an MD run carried out in the NVE ensemble with  $\sigma/k_B = 9000 \text{ K}$ . The run remained in a solid state after more than 50 ps and the average temperature is close to the estimated  $T_h$  (which is 8623 K) reported in Table S2.

**Table S1**

Melting points for Ca-perovskite

Method	T K	p GPa	dT/dp K/GPa	$\rho$ g/cm <sup>3</sup>	Ts kJ/g	Phase assemblage	Time ps
<b>TI</b>	2500	17.9 +11.3/-3.1	129.3	3.363 (L) 4.077 (S)	7.7136 (L) 6.7068 (S)		
	6000	84.4 +16.5/-14.2	26.3	4.417 (L) 4.752 (S)	24.1196 (L) 20.4783 (S)		
<b>2PT</b>	2500	21.0	91.5	3.456 (L) 4.144 (S)	7.973 (L) 6.660 (S)		
	4000	49.9	39.1	4.053 (L) 4.462 (S)	14.492 (L) 12.177 (S)		
	6000	133.4	13.6	5.047 (L) 5.278 (S)	23.413 (L) 19.584 (S)		
<b>LCC</b>	2500	17.5 ± 0.7		3.54		S+ L	160.5
	2500	18.6 ± 1.4		3.73		S+L	100*
	3000	19.9 ± 0.8		3.54		L	52.1
	3000	21.2 ± 0.8		3.83		S+L	148.7
	5000	117.9 ± 1.3		5.15		S (w glass cluster)	38.0
	5500	119.8 ± 1.3		5.15		S (w glass cluster)	60.0
	6000	101.4 ± 1.4		4.92		S (w few defects)	54.9
	6250	115.0 ± 1.3		5.07		S (w cryst defects)	169.5
	6500	117.8 ± 1.3		5.07		S (w cryst defects)	102.2
	6750	116.0 ± 1.7		4.92		S+L	100.0*
	6750	117.4 ± 1.3		5.07		S (w single defect)	143.8
	7000	125.9 ± 2.0		4.95		L	12.1
	7000	134.4 ± 1.8		5.04		L	51.4
	7000	136.5 ± 2.0		5.07		L	25.8
	7000	137.2 ± 1.6		5.07		L	105.7
	7000	131.7 ± 1.6		5.10		S+L	131.8
	7000	134.9 ± 1.6		5.15		S+L	142.8
	7500	127.8 ± 1.6		4.93		L	3.1
<b>SCC</b>	2089	14.0					2-15
	4623	42.0					3-23
	5700	70.0					3-27
	7001	120.0					2-17

Methods abbreviations: solid-liquid, large-cell coexistence (LCC) and small-cell coexistence (SCC), thermodynamic integration (TI) and two-phase thermodynamics (2PT). Reconnaissance simulations to investigate the cell size effects for the solid-liquid SCC method and some of the large-cell coexistence (LCC) simulations far above and below the melting curve are not reported. The pressure fluctuations ( $\pm 1\sigma$ ) reported for the LCC simulations represent the last 200 steps. The  $2\sigma$  temperature error-bars for the SCC calculations, shown in Fig. 1, are from a statistical distribution of the number of simulations ending in a solid or a liquid state. Other abbreviations: Ts, total entropy multiplied by temperature; L, liquid; S, solid; cryst, crystalline; w, with. The presence of crystalline defects where e.g. Ca and Si have exchanged sites and frozen-in glass-like clusters embedded in a solid crystalline matrix, illustrated in Fig. S1, are indicated in the phase assemblage column. \*Two simulations terminated after 100 ps are marked by stars.



**Table S2**

Calculated homogeneous and equilibrium melting temperatures using the Z-method with different choices of Fermi-Dirac smearing-parameter,  $\sigma$ .

p (GPa)	$T_h$ (K)	$T_m$ (K)	$T_{m-\tau_w}$ (K)	$T_{cl} = \sigma/k_B$ (K)	Functional	Reference
$103.0 \pm 0.2$	7120 (40)	not provided	5200 (30)	not provided	PBEsol	B&S (2019)
$105 \pm 3.3$	8806	6659	6493	updated	PBEsol	This study
$104.8 \pm 2.6$	8585	6589	not calc.	updated	PBE	This study
$105.5 \pm 2.8$	8757	6505	not calc.	9000	PBE	This study

MD runs labelled "updated" are those where the Fermi-Dirac smearing was adjusted at about every 1 ps to match the average temperature in the previous run, as explained in Section S2. Reference B&S (2019): Braithwaite and Stixrude (2019). The waiting time analysis was performed with the PBEsol functional at 105 GPa, only. The listed  $T_m$  and  $T_{m-\tau_w}$  are without and with the waiting time analysis, respectively.